

**SIMULATION OF A HOLOGRAPHIC 3-D TELEVISION  
DISPLAY**

**A THESIS**

**SUBMITTED TO THE DEPARTMENT OF ELECTRICAL AND  
ELECTRONICS ENGINEERING  
AND THE INSTITUTE OF ENGINEERING AND SCIENCES  
OF BILKENT UNIVERSITY  
IN PARTIAL FULFILLMENT OF THE REQUIREMENTS  
FOR THE DEGREE OF  
MASTER OF SCIENCE**

**By**

**Gözde BOZDAĞI  
December 1990**

*thesis*  
**TA  
1540  
.B69  
1990**

# SIMULATION OF A HOLOGRAPHIC 3-D TELEVISION DISPLAY

A THESIS

SUBMITTED TO THE DEPARTMENT OF ELECTRICAL AND  
ELECTRONICS ENGINEERING  
AND THE INSTITUTE OF ENGINEERING AND SCIENCES  
OF BILKENT UNIVERSITY  
IN PARTIAL FULFILLMENT OF THE REQUIREMENTS  
FOR THE DEGREE OF  
MASTER OF SCIENCE

By

Gözde Bozdağı

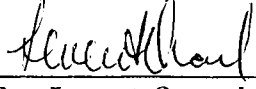
December 1990

Gözde Bozdağı  
tarafından bağlanmıştır.

TA  
1540  
.069  
1990

B-7782

I certify that I have read this thesis and that in my opinion it is fully adequate, in scope and in quality, as a thesis for the degree of Master of Science.



Assoc. Prof. Dr. Levent Onural (Principal Advisor)

I certify that I have read this thesis and that in my opinion it is fully adequate, in scope and in quality, as a thesis for the degree of Master of Science.



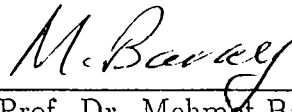
Prof. Dr. Abdullah Atalar

I certify that I have read this thesis and that in my opinion it is fully adequate, in scope and in quality, as a thesis for the degree of Master of Science.



Assist. Prof. Dr. Ender Ayanoglu

Approved for the Institute of Engineering and Sciences:



Prof. Dr. Mehmet Baray  
Director of Institute of Engineering and Sciences

## ABSTRACT

### SIMULATION OF A HOLOGRAPHIC 3-D TELEVISION DISPLAY

Gözde Bozdağı

M.S. in Electrical and Electronics Engineering

Supervisor: Assoc. Prof. Dr. Levent Onural

December 1990

The theory and the computer simulations of an *acousto-optical holographic 3-D television display* are presented in this dissertation. The technique used is based on the reproduction of the desired pattern, in our case the hologram, using traveling surface waves. The crystal that will be used as the medium of display is assumed to have a number of electrodes attached to it on one side. If signals are applied to all of the electrodes, propagating waves from the electrodes will superpose to form a time-varying surface field pattern on the crystal. It is possible to find out the signals to be applied to the electrodes through an inversion relationship from the original holographic pattern. The proposed method is simpler and more efficient than the methods available in the literature and it solves the display resolution problem completely.

*Keywords:* Off-axis holograms, coordinate transformation, interpolation, simulation, 3-D television.

# ÖZET

## 3 BOYUTLU HOLOGRAFİK TELEVIZYON SİMÜLASYONU

Gözde Bozdağı

Elektrik ve Elektronik Mühendisliği Bölümü Yüksek Lisans

Tez Yöneticisi: Doç. Dr. Levent Onural

Aralık 1990

Bu çalışmada yeni bir 3-boyutlu holografik görüntüleme sisteminin teorisi verilmiş ve bilgisayar simülasyonları yapılmıştır. Kullanılan teknik, istenilen şeklin ilerleyen yüzey dalgaları sayesinde bir kristal üzerinde oluşturulmasına dayanmaktadır. Elektrodlara uygulanan sinyaller tamamıyla girişteki holografik şekilden elde edilebilmektedir. Bu sinyallerin yarattığı yüzey dalgaları zaman içinde ilerleyerek ve üst üste binerek istenilen anda istenilen görüntünün oluşmasını sağlarlar. Kullanılan sistemlerden daha basit ve etkili olan bu metod aynı zamanda görüntülemedeki çözümleme problemini de ortadan kaldırmaktadır.

*Anahtar sözcükler:* Çift ışınlı hologramlar, koordinat dönüşümü, simülasyon, interpolasyon, 3 boyutlu televizyon.

## ACKNOWLEDGEMENT

I would like to thank Assoc. Prof. Dr. Levent Onural for his supervision, guidance, suggestions, and encouragement throughout the development of this thesis.

I am also indebted to Prof. Abdullah Atalar for his helps in shaping the project in its early stages.

I would also like to gratefully acknowledge the other member of my M.S. Thesis Committee: Assist. Prof. Dr. Ender Ayanoglu.

Finally, it is my pleasure to express my thanks to Ogan Ocalı for his valuable discussions and to my family for providing morale support during this study.

## FOREWORD

This thesis contains the computer simulations of the invention “*An Acousto-Optical Holographic 3-D TV Display*” registered with the US Patent Office in Disclosure Document number 225219.

# Contents

<b>1</b>	<b>INTRODUCTION</b>	<b>1</b>
1.1	Stereoscopy . . . . .	1
1.2	Holography . . . . .	2
1.3	History of Holography	2
1.4	Three-Dimensional Television Systems . . . . .	3
<b>2</b>	<b>MATHEMATICAL MODEL FOR OFF-AXIS HOLOGRAPHY</b>	<b>6</b>
2.1	Introduction . . . . .	6
2.2	Continuous Domain Modeling . . . . .	6
2.2.1	Recording . . . . .	6
2.2.2	Reconstruction . . . . .	9
2.3	Discrete Model . . . . .	13
2.4	Results . . . . .	15

<i>CONTENTS</i>	viii
<b>3 WAVE PROPAGATION</b>	<b>17</b>
3.1 Introduction . . . . .	17
3.2 Propagation of an Arbitrary Wave . . . . .	17
3.3 Superposition of Waves . . . . .	18
<b>4 GENERATION OF TIME SIGNALS BY COORDINATE TRANSFORMATION</b>	<b>20</b>
4.1 Introduction . . . . .	20
4.2 Inversion Relationship . . . . .	20
4.3 Digital Processing . . . . .	28
4.4 Results . . . . .	35
<b>5 A PRACTICAL IMPLEMENTATION</b>	<b>44</b>
<b>6 RESULTS</b>	<b>46</b>
<b>7 HOW TO USE THE SIMULATOR</b>	<b>55</b>
7.1 Example . . . . .	55
<b>8 CONCLUSION</b>	<b>58</b>
<b>A FOURIER TRANSFORM PROPERTIES</b>	<b>60</b>

*CONTENTS*

ix

**B CALCULATION OF THE DISCRETE FOURIER TRANSFORM 61**

**C STANDARD INPUT/OUTPUT FORMAT 64**

## List of Figures

2.1	Off-axis hologram recording . . . . .	7
2.2	Two-dimensional system model for hologram recording . . . . .	9
2.3	Hologram reconstruction . . . . .	10
2.4	Reconstruction from the off-axis hologram . . . . .	12
2.5	Discrete implementation of the continuous system given in Fig.2.2 .	14
2.6	Discrete implementation of the continuous system given in Fig.2.4 .	15
2.7	An object and the simulated off-axis hologram of it . . . . .	16
2.8	Reconstruction from the hologram in Fig.2.7 . . . . .	16
3.1	Superposition of waves . . . . .	19
4.1	Time-varying field $e^{j(\omega t - k_x x + u y)}$ at $t = 0$ . . . . .	22
4.2	$\Psi(\Omega_x, \Omega_y)$ with a rectangular pass-band. (Taken from [7] with the permission of the author) . . . . .	26

4.3	$F(\omega, u)$ after coordinate transformation. (Taken from [7] with the permission of the author) . . . . .	26
4.4	$F(\omega, u)$ with a rectangular pass-band. (Taken from [7] with the permission of the author) . . . . .	27
4.5	$\Psi(\Omega_x, \Omega_y)$ after inverse coordinate transformation. (Taken from [7] with the permission of the author) . . . . .	27
4.6	Sample locations after and before transformation	29
4.7	Interpolation . . . . .	34
4.8	Input object pattern . . . . .	37
4.9	Computed time signals after extension to 128x128 image . . . . .	37
4.10	Computed time signals after extension to 256x256 image . . . . .	38
4.11	Reconstructed objects (a)by radiating the time signal in Fig.4.9,(b)by radiating the time signal in Fig.4.10, (c)by periodically radiating the time signals in Fig.4.10 . . . . .	38
4.12	Input object pattern and reconstructed object after radiation of time signal in Fig.4.13 . . . . .	39
4.13	Computed time signals . . . . .	39
4.14	Another input object pattern and reconstructed object after radiation of time signal in Fig.4.15 . . . . .	40
4.15	Computed time signals . . . . .	40
4.16	Input pattern to show the relation between the resolution and the electrode number . . . . .	41

4.17	Computed time signals for 128 electrodes . . . . .	41
4.18	Computed time signals for 256 electrodes . . . . .	42
4.19	Reconstructed object after radiation of time signal in Fig.4.17 . . .	42
4.20	Reconstructed object after radiation of time signal in Fig.4.18 . . .	43
5.1	A practical implementation . . . . .	45
6.1	(a)The 64x128 2D <i>flower</i> pattern and (b)the simulated hologram of this pattern . . . . .	48
6.2	The computed time signal . . . . .	48
6.3	The reconstructed hologram after radiation of time signal in Fig.6.2	49
6.4	Reconstruction from holograms (a)in Fig.6.1.b and (b)in Fig.6.3 . .	49
6.5	(a)Another input pattern and (b)the simulated hologram of this pattern . . . . .	50
6.6	The computed time signal . . . . .	50
6.7	The reconstructed hologram after radiation of time signal in Fig.6.6	51
6.8	Reconstruction from holograms (a)in Fig.6.5.b and (b)in Fig.6.7 . .	51
6.9	(a)A 3D input pattern and (b)the simulated hologram of this pattern	52
6.10	The computed time signal . . . . .	52
6.11	The reconstructed hologram after radiation of time signal in Fig.6.10	53

6.12 Reconstruction of the two objects at different depths from the holo- gram in Fig.6.9.b . . . . .	53
6.13 Reconstruction of the two objects at different depths from the holo- gram in Fig.6.11 . . . . .	54

# Chapter 1

## INTRODUCTION

The display of three-dimensional information is central to progress in many fields, such as medical imaging, computer-aided design, and navigation. Two well-known techniques for three dimensional display are stereoscopy and holography [12],[18],[23].

### 1.1 Stereoscopy

Stereoscopy is based on the psychological nature of perception. Although the underlying principles are not known, it has been known for more than a century that the perception of the three-dimensional environment is partially because of the difference of the views seen by the right and the left eyes. Therefore, any recording system which records a scene from two different proper angles, and a means to transfer each image to the corresponding eye, will generate a three-dimensional perception. The technique has developed pretty well, and the commercial 3-D motion pictures have long been available, even in full color. A major drawback of stereoscopy is the lack of proper parallax in the vertical direction. Stereoscopy does not give a true three-dimensional display.

## 1.2 Holography

Holography is a true three-dimensional method. Furthermore, it is not based on the psychology of perception, but rather on the physics of optical waves. When an observer looks at the three-dimensional environment, what is seen is the optical light arriving at the eye. In holography, the information-carrying optical waves which come from the three-dimensional environment are somehow duplicated in the absence of the original source. Ideally, if the reconstructed light is exactly the same as the original, their impact at the observer will also be the same. Therefore, an observer will see the same three-dimensional environment, whether he/she looks at the light from the original or its duplicate. Because of this, it is normal for an observer to feel disbelief when he sees his first hologram. Holograms can be easily understood by using simple optical and mathematical principles.

## 1.3 History of Holography

Holography was invented by the Hungarian-born British scientist Dennis Gabor, and introduced as “a new two-step method for optical imagery,” in 1948 [13]. By this invention, for the first time in history, a practical method of storing and retrieving phase information of a wave was formulated. Even though the validity of Gabor’s idea was confirmed by a number of workers, it did not get the attention it deserved for many years. The main reasons for the lack of progress was the poor quality of holographic images and the lack of a suitable source of light having the property known as coherence. The poor quality was largely due to the presence of the conjugate image as well as scattered light from the direct beam, both of which were superposed on the reconstructed image. Several techniques were proposed to eliminate the conjugate image but none was really successful. At the same time, the limited coherence of the source restricted the holographic images to transparencies little larger than a pinhead. As a result, interest in holography declined after a few years [18].

The breakthrough which effectively solved the twin-image problem and opened the way to the large scale development of holography was the off-axis reference beam technique developed by Leith and Upatnieks in 1961. They argued that the conjugate image was essentially due to aliasing, and introduced a spatial carrier frequency by using a separate reference wave which was incident on the photographic plate at an appreciable angle with respect to the object wave [11]. Such a hologram, when illuminated with the original reference beam, produced a pair of images which were separated by a large enough angle from the directly transmitted beam and from each other to ensure that they did not overlap. The importance of Leith and Upatnieks' work lies in their fundamental approach to the problem of holography, by describing the process from a communication theory viewpoint. They have shown that construction of hologram constitutes a sequence of three well-known operations: modulation, frequency dispersion or defocusing, and square-law detection. In the reconstruction process an inverse-frequency-dispersion or focusing operation is carried out.

The contribution of Leith and Upatnieks to holography was followed by the development of laser. This made available for the first time a powerful source of highly coherent light and made it possible to record holograms of diffusely reflecting objects with appreciable depth [13].

These advances set off an explosive growth of activity and optical holography soon found a very large number of scientific applications. These included high-resolution imaging of aerosols [Thompson, 1967], multiple imaging [Lu, 1968], computer generated holograms [Lohmann and Paris, 1967], information storage [Stroke and Restruck, 1965], character recognition [Vander Lugt, 1965], holographic interferometry [Brooks, Burch, Collier, and Powell, 1965] [18],[19].

## 1.4 Three-Dimensional Television Systems

The invention of holography has also sparked hopes for a three-dimensional electronic imaging system analogous to television. In principle one should be able to

form a hologram pattern over television channels, and replicate the hologram at the receiving station. When the replica is illuminated with a laser light, it will allow the reconstructed wave to emerge and generate the desired image.

Some three-dimensional television systems, including both the camera and the display ends, are reported in literature but the display problems of 3-D moving imagery effectively prevents their commercial development [7],[18],[19],[21],[22]. Some of these 3-D television systems are holographic systems, whereas others are based on stereoscopic imaging. For example, in a reported system, the receiver gets the electrical video signal which represents the hologram and forms the hologram on a cathode ray tube. This hologram is then imaged onto an optical-to-optical transducer called a liquid crystal light valve, and a coherent source forms the three-dimensional field reconstruction from the hologram [7],[18]. In this system the resolution at the display end is limited to resolution of the optical-to-optical transducer. Although nowadays optical-to-optical transducers are also starting to be produced in the resolution range suitable for holographic display, the trade-off between the resolution and refresh rate still remains as a problem. In another system, a photoconductor-thermoplastic transducer is used to duplicate the transmitted hologram. The problem with this system is again the refresh rate which is not enough for 3-D moving imagery. Acousto-optic modulators are also used for display purposes in holographic systems [21],[22]. In these systems the coherent light is modulated by the acousto-optic modulator and optically processed to produce a 3-D image with horizontal parallax. The display resolution problem is tried to be solved by methods such as elimination of horizontal or vertical parallax, scan of a relatively small modulator image.

In this dissertation, we present a new technique for the display end of a holographic three-dimensional television system which solves the display resolution problem completely. The technique is based on the reproduction of the hologram using traveling surface waves. Thus, the technique proposed in this dissertation is conceptually different than the previous ones which use the direct scanning of the hologram. The SAW device that will be used as a medium of display is assumed to have an array of electrodes attached to it. An electrical signal applied to any one of these electrodes will generate an acoustical wave propagating on the surface

of the crystal where the electrodes are the sources. If signals are applied to all of the electrodes, propagating waves from the electrodes will superpose to form a time-varying surface field pattern on the crystal. This pattern is the hologram itself. It is possible, through an inversion relationship, to find out the signals to be applied to all of the electrodes, in order to have a specified field pattern on the crystal surface at a specified time instant. The inversion relationship is derived from the underlying physics.

We begin in Chapter 2 with mathematical models for off-axis holography, both continuous and discrete cases are given. Chapter 3 is the derivation of a general radiation formula by using simple wave concepts. In Chapter 4, the proposed inversion relationship is explained. Included in this section is the discrete implementation of the inversion relationship. Chapter 5 gives a practical implementation of the proposed method and Chapter 6 gives the simulation results. Chapter 7 is a guide showing how to use the simulator. Finally, Chapter 8 gives the conclusion.

## Chapter 2

# MATHEMATICAL MODEL FOR OFF-AXIS HOLOGRAPHY

### 2.1 Introduction

Mathematical models for continuous off-axis holography can be found in the literature (for example [4],[10],[11]). The systems approach, which models the physical phenomena using filters and other elements which have an input-output description, is used in this dissertation for Fresnel off-axis holography.

### 2.2 Continuous Domain Modeling

#### 2.2.1 Recording

The mathematical model given in this section is based on the simplified diagram of Fig.2.1. A laser beam is split into the object beam which illuminates the object, and the reference beam which illuminates the recording medium directly. The recording of the superposition of the object beam  $O$  and the reference beam  $R$  is

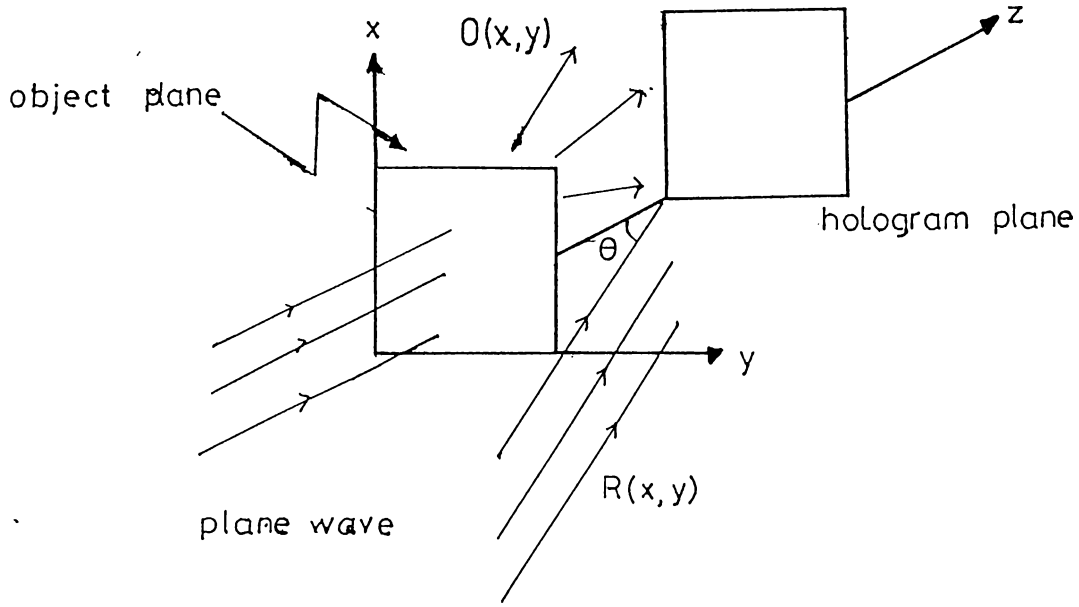


Figure 2.1: Off-axis hologram recording

a hologram.

Assume that the reference beam is a plane wave with amplitude  $R_o$ , and it is incident upon the photographic plate with its direction of propagation in the  $x-z$  plane as shown in Fig.2.1. Then,  $R(x, y)$  can be expressed as,

$$R(x, y) = R_o e^{jkx \sin(\theta)} e^{jkz}. \quad (2.1)$$

The field  $O(x, y)$  can be calculated by using the Fresnel approximation [4]. Let the object be made up of slices of vanishingly thin in the  $z$ -direction. The field diffracted from only one of the object slices,  $a(x, y)$ , located in the plane  $z = 0$ , is considered first. When such a field is observed at a fixed distance  $z$  the field distribution is expressed by

$$O(x, y) = \frac{B}{j\lambda z} e^{j\frac{2\pi}{\lambda}z} \int_{-\infty}^{\infty} \int_{-\infty}^{\infty} a(\alpha, \beta) \times e^{j\frac{\pi}{\lambda z}[(x-\alpha)^2 + (y-\beta)^2]} d\alpha d\beta. \quad (2.2)$$

The above equation can be written as

$$O(x, y) = a(x, y) ** h_z(x, y), \quad (2.3)$$

where \*\* denotes two-dimensional convolution and  $h_z(x, y)$  is defined by

$$h_z(x, y) = \frac{1}{j\lambda z} e^{j\frac{\pi}{\lambda z}(x^2+y^2)}, \quad (2.4)$$

by assuming the amplitude of the incident plane wave  $B$  to be 1 and by dropping the phase term  $e^{j\frac{2\pi}{\lambda}z}$ . The reason for dropping the phase term is due to the fact that only the magnitude of the field is considered in the hologram formation.

By using Eq.2.2 and Eq.2.3 the field distribution at a distance  $z$  from the object plane is written as

$$\begin{aligned} \Psi_z(x, y) &= O(x, y) + R(x, y) \\ &= R_o e^{jkx \sin(\theta)} + a(x, y) ** h_z(x, y). \end{aligned} \quad (2.5)$$

The intensity of  $\Psi_z(x, y)$  is recorded as the hologram,  $I_z(x, y)$ , i.e.,

$$\begin{aligned} I_z(x, y) &= \Psi_z(x, y)\Psi_z^*(x, y) \\ &= R_o^2 + |a(x, y) ** h_z(x, y)|^2 + R_o e^{-jkx \sin(\theta)} [a(x, y) ** h_z(x, y)] + \\ &\quad R_o e^{jkx \sin(\theta)} [a^*(x, y) ** h_z^*(x, y)]. \end{aligned} \quad (2.6)$$

Since the field is represented as a two-dimensional convolution, it can be modeled as the output of a two-dimensional linear system, where the system impulse function is  $h_z(x, y)$ . The block diagram of the system corresponding to hologram recording is shown in Fig.2.2.

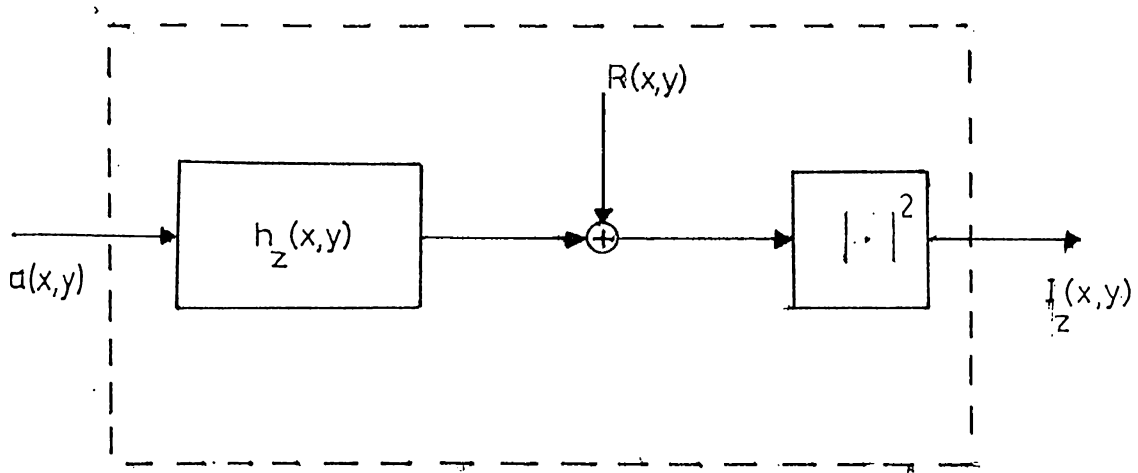


Figure 2.2: Two-dimensional system model for hologram recording

In Eq.2.6, the first term is related to the uniform beam of light and the second term is the cross-term, which is not desirable. The convolution with kernel  $h_z(x, y)$  is an operation which disperses the energy of a space-limited smooth object  $a(x, y)$  to a wider region in the  $x, y$  plane (wider as  $z$  becomes large). If the energy of  $a(x, y)$  is limited, then the energy of the linear terms in Eq.2.5 drops much below 1. Therefore, the squares of these small values (the cross-term) are negligible. The significant terms are the second and the third terms which contain the factor  $a(x, y)$  and pertain to the image.

## 2.2.2 Reconstruction

The image is reconstructed by illuminating the hologram with a reconstruction beam  $P(x, y)$  [4]. This beam is assumed to be a plane wave incident upon the hologram, tilted again only in the  $x$ -direction at an angle  $\theta_p$ , as shown in Fig.2.3. If the object is wanted to be reconstructed at its original location, then  $P(x, y)$  must be equal to  $R(x, y)$ , i.e.,  $\theta_p = \theta$ . From now on we will consider this case only.

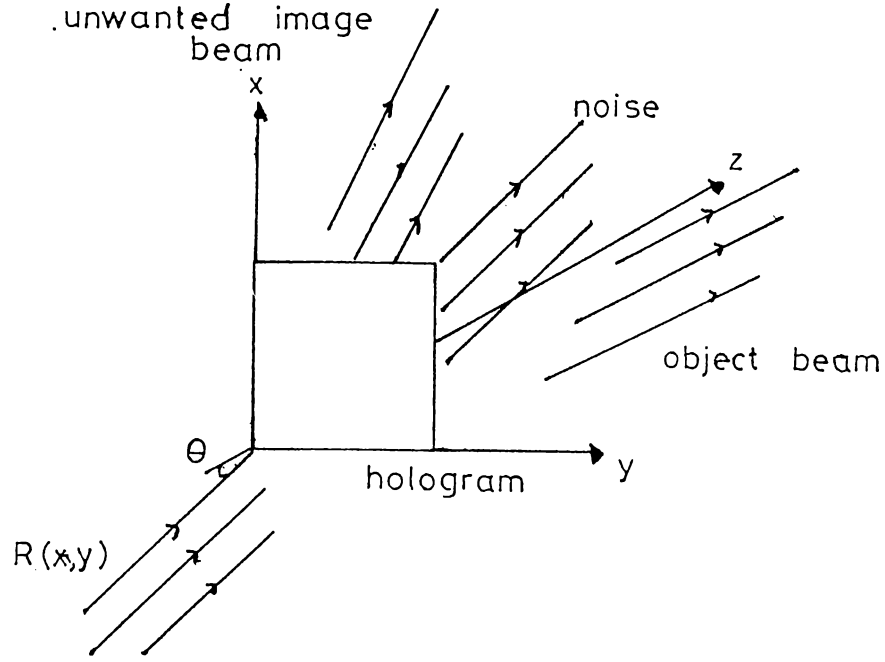


Figure 2.3: Hologram reconstruction

The Fresnel diffraction pattern of the illuminated hologram is

$$\Psi_{rec}(x, y) = [R(x, y)T(x, y)] * * h_{zi}(x, y) \quad (2.7)$$

where  $T(x, y)$  is a function of  $I(x, y)$  depending on the kind of the hologram.

In general, holograms can be recorded as amplitude or phase variations [12]. In the amplitude hologram, the interference pattern between the object and the reference wave is recorded as the amplitude reflection factor of the recording medium. In this case, the field after reconstruction becomes

$$\Psi_{rec}(x, y) = [R(x, y)I(x, y)] * * h_{zi}(x, y). \quad (2.8)$$

In the phase hologram, the interference fringes are recorded as the variation of the thickness or refractive index of the recording medium. In this case, the field after reconstruction becomes

$$\Psi_{rec}(x, y) = [R(x, y)e^{jI(x, y)}] ** h_z(x, y). \quad (2.9)$$

For  $|I(x, y)| \ll 1$ , the Eq.2.9 becomes

$$\Psi_{rec}(x, y) = [R(x, y)(1 + jI(x, y))] ** h_z(x, y).$$

So we can approximate the reconstructed field as

$$\Psi_{rec}(x, y) = [R(x, y)I(x, y)] ** h_z(x, y). \quad (2.10)$$

By using Eq.2.10 and Eq.2.6 we can express the field as

$$\begin{aligned} \Psi_{rec}(x, y) = & R_o^4 e^{jkx \sin(\theta)} ** h_z(x, y) + \\ & R_o [e^{jkx \sin(\theta)} |a(x, y) ** h_z(x, y)|^2] ** h_{z_i}(x, y) + \\ & R_o^2 [e^{j2kx \sin(\theta)} a^*(x, y) ** h_z^*(x, y)] ** h_{z_i}(x, y) + \\ & R_o^2 a(x, y) ** h_z(x, y) ** h_{z_i}(x, y). \end{aligned} \quad (2.11)$$

If  $z_i = -z$  we can simplify Eq.2.11 by using the following properties of the convolution kernel  $h_z(x, y)$  [14]:

$$h_{-z}(x, y) = h_z^*(x, y) \quad (2.12)$$

$$h_z(x, y) ** h_z^*(x, y) = \delta(x, y) \quad (2.13)$$

$$h_z(x, y) ** h_z(x, y) = h_{2z}(x, y). \quad (2.14)$$

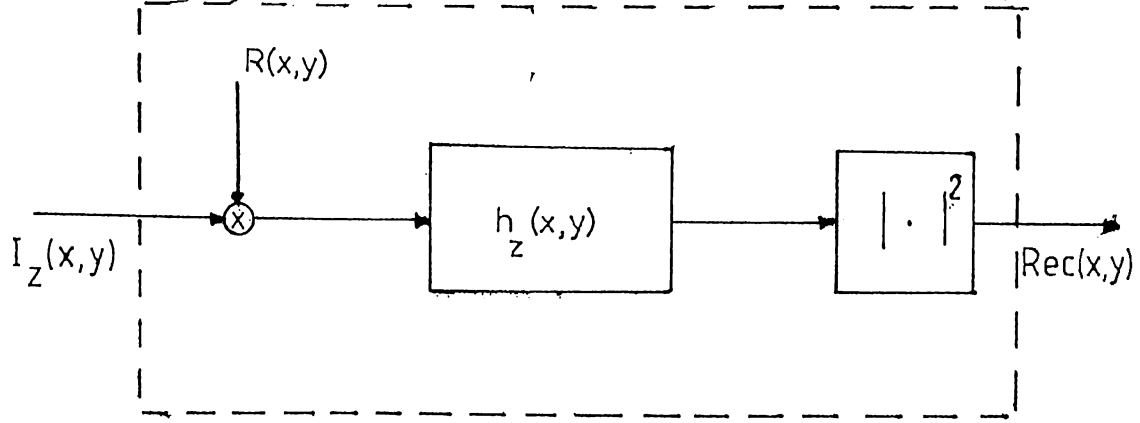


Figure 2.4: Reconstruction from the off-axis hologram

Therefore, the field after reconstruction,  $\Psi_{rec}(x, y)$ , is

$$\begin{aligned}
 \Psi_{rec}(x, y) &= R_o^4 e^{jk_x \sin(\theta)} * h_z(x, y) \\
 &+ R_o [e^{jk_x \sin(\theta)} |a(x, y) * h_z(x, y)|^2] * h_z^*(x, y) \\
 &+ R_o^2 a(x, y) + R_o^2 e^{j2k_x \sin(\theta)} a^*(x, y) * h_{2z}^*(x, y) \quad (2.15)
 \end{aligned}$$

In Eq.2.15, the first term is the uniform beam of light which propagates straight through the hologram. The second term is the undesired cross term artifact. The third term is the desired reconstruction, and the fourth term is the field of the hologram of the object distribution  $a(x, y)$  at a distance  $2z$  and with a shift in the  $x$ -direction.

In some non-optical reconstructions (such as digital) it may be possible to record the field; but in optical reconstruction the magnitude square operation is unavoidable [15].

As in the recording step, we can model the reconstruction process by a two-dimensional system as in Fig.2.4.

### 2.3 Discrete Model

Let's consider the system given in Fig.2.2. A discrete impulse function  $h_{z_D}(n, m)$  must be determined corresponding to the continuous impulse function  $h_z(x, y)$ . In [14] a detailed analysis of sampling of  $h_z(x, y)$  to get  $h_{z_D}(n, m)$  is given, so only the results will be mentioned here.

The discrete impulse response  $h_{z_D}(n, m)$  is given by

$$h_{z_D}(n, m) = \begin{cases} h_z(Xn, Ym) & \text{if } |n| \leq \frac{N_h-1}{2}, |m| \leq \frac{M_h-1}{2} \\ 0 & \text{elsewhere} \end{cases} \quad (2.16)$$

where  $N_h$  and  $M_h$  give the discrete size of the filter in dimensions  $n$  and  $m$  respectively.

The input function can also be discretized similarly to yield

$$a_D(n, m) = a(Xn, Ym).$$

In our implementations, we chose  $X = Y$ , i.e.,  $N = M$ . For the purpose of normalization, a new variable  $\alpha$ , which is related to the sampling of the optical hologram, is introduced [14], such that

$$\alpha^2 \frac{\pi}{N} = \frac{\pi}{\lambda z} X^2. \quad (2.17)$$

So, we have

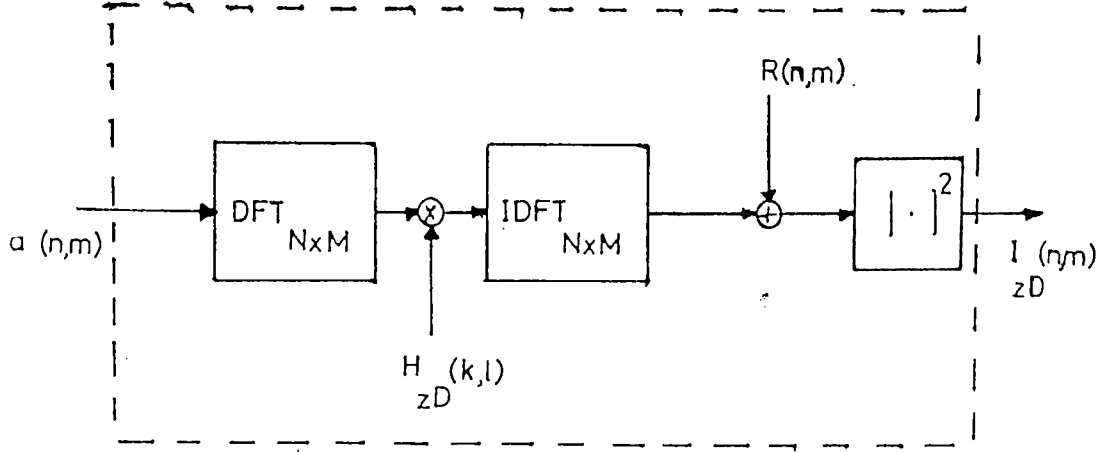


Figure 2.5: Discrete implementation of the continuous system given in Fig.2.2

$$h_{zD}(n, m) = e^{j\frac{\pi}{\lambda z}X^2(n^2+m^2)} = e^{j\alpha^2\frac{\pi}{N}(n^2+m^2)}. \quad (2.18)$$

We define another variable  $\beta$  for the reference beam where

$$\beta = 2\pi\alpha \cos(\theta)\sqrt{\frac{\lambda z}{N}}. \quad (2.19)$$

Now the discrete field can be written as

$$\Psi_{zD}(n, m) = R_0 e^{j\beta n} + a(n, m) ** h_{zD}(n, m). \quad (2.20)$$

Similar operations can be done for the reconstruction case. In order to increase computational efficiency, circular convolution can be carefully used instead of linear convolution in Eq.2.20. So we can show the discrete implementations of the continuous systems given in Fig.2.2 and Fig.2.4 as in Fig.2.5 and Fig.2.6.

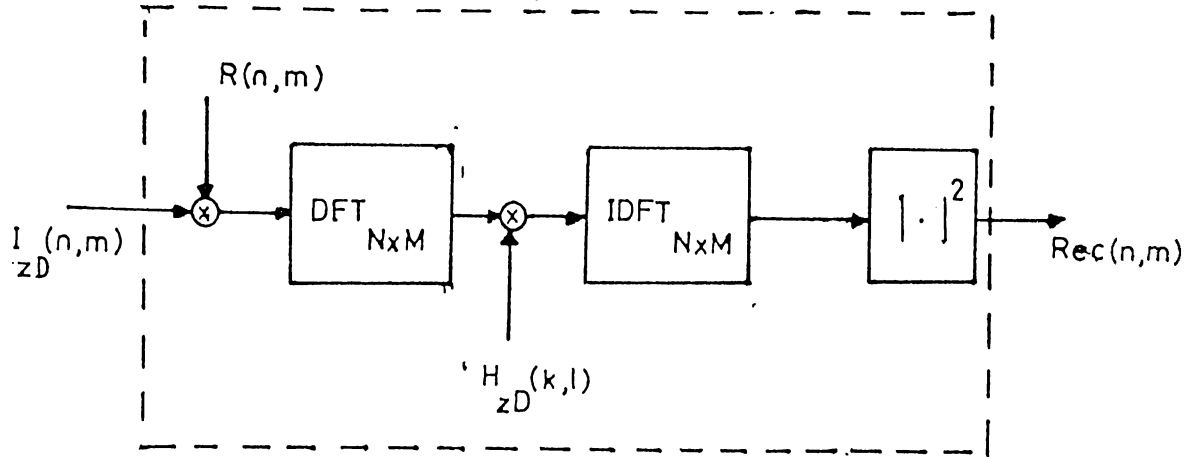


Figure 2.6: Discrete implementation of the continuous system given in Fig.2.4

## 2.4 Results

In the simulations,  $N$  and  $M$  are taken to be 128. Gray level variations are quantized to 256 levels: 0 is the darkest and 255 is the brightest. The amplitude of the reference beam,  $R_o$ , is 200 in order to decrease the effect of the cross term in Eq.2.6. At the reconstruction step the DC component is suppressed to decrease the effect of the uniform beam of light propagating directly through the hologram.

Fig.2.7 shows a synthesized object and the simulated off-axis hologram of it. If the hologram is reconstructed by using Eq.2.10, we get Fig.2.8.

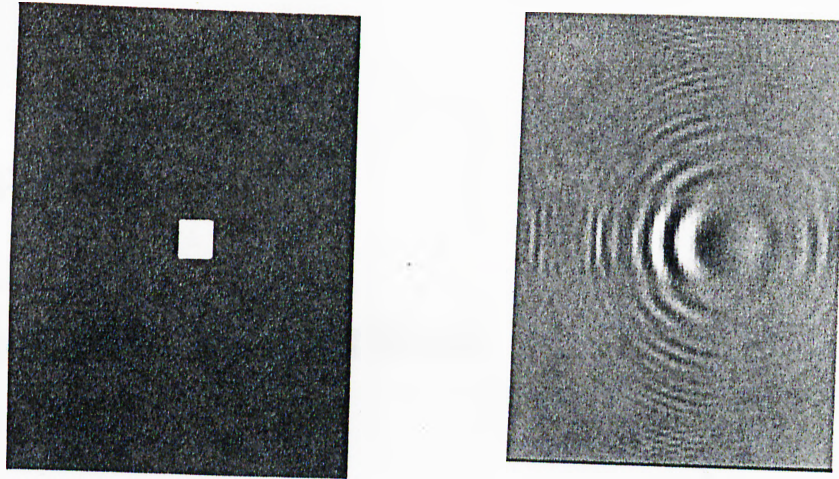


Figure 2.7: An object and the simulated off-axis hologram of it

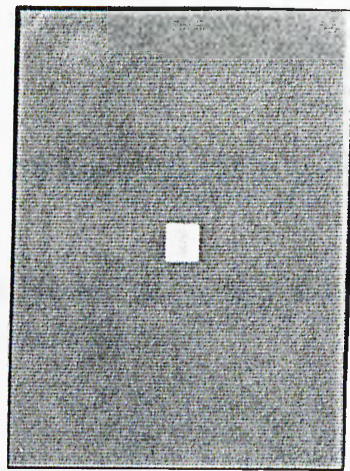


Figure 2.8: Reconstruction from the hologram in Fig.2.7

## Chapter 3

# WAVE PROPAGATION

### 3.1 Introduction

In this chapter we try to find an input-output relationship if we have an array of electrodes, each with a different input, attached to one side of a crystal to form an output surface wave pattern on the crystal.

### 3.2 Propagation of an Arbitrary Wave

If we have a point source located at  $(x_o, y_o)$  and oscillating with respect to time as  $e^{j\omega t}$ , the field on the surface becomes

$$E(t, r) = \frac{E_o}{((x - x_o)^2 + (y - y_o)^2)^{\frac{1}{2}}} e^{j\omega(t - \frac{\sqrt{(x-x_o)^2 + (y-y_o)^2}}{c})}. \quad (3.1)$$

Now, consider a source whose variation with respect to time is  $x(t)$ . From Fourier transform relationships,  $x(t)$  can be written in terms of the superposition of complex sinusoids as

$$x(t) = \frac{1}{2\pi} \int_{-\infty}^{\infty} X(\omega) e^{j\omega t} d\omega.$$

So, by using Eq.3.1 the resultant field of  $x(t)$  becomes

$$E(t, r) = \frac{1}{2\pi} \int_{-\infty}^{\infty} \frac{E_o X(\omega)}{((x - x_o)^2 + (y - y_o)^2)^{\frac{1}{2}}} e^{j\omega(t - \frac{\sqrt{(x-x_o)^2 + (y-y_o)^2}}{c})} d\omega. \quad (3.2)$$

If we take the constant terms out of the integral and use the Fourier Transform properties (App.A) we get

$$\begin{aligned} E(t, r) &= \frac{E_o}{2\pi((x - x_o)^2 + (y - y_o)^2)^{\frac{1}{2}}} \int_{-\infty}^{\infty} X(\omega) e^{j\omega(t - \frac{\sqrt{(x-x_o)^2 + (y-y_o)^2}}{c})} d\omega \quad (3.3) \\ &= \frac{E_o}{2\pi((x - x_o)^2 + (y - y_o)^2)^{\frac{1}{2}}} x\left(t - \frac{\sqrt{(x - x_o)^2 + (y - y_o)^2}}{c}\right). \quad (3.4) \end{aligned}$$

The above equation shows that the resultant field will be the delayed and scaled version of the input.

### 3.3 Superposition of Waves

As shown in the preceding section, we can find the resultant field due to any arbitrary oscillating source. Now, if we have more than one point source, what will the resultant field be? The answer is the superposition of individual fields, assuming linearity of the media [8].

We will find the actual field at any point by adding the fields due to each individual source. So, if we have  $(k + 1)$  sources located along  $y$  and at  $x = 0$  as shown in Fig.3.1, then the total field will be

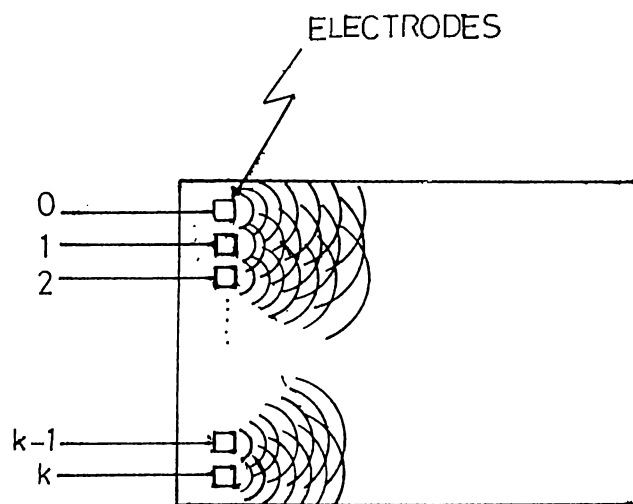


Figure 3.1: Superposition of waves

$$E(t, r) = \sum_{i=0}^k E(t, r_i).$$

where  $r_i = \sqrt{x^2 + (y - y_i)^2}$  and  $y_i$  shows the source location along  $y$ .

So

$$E(t, r) = \sum_{i=0}^k \frac{E_o}{2\pi(x^2 + (y - y_i)^2)^{\frac{1}{2}}} x\left(t - \frac{\sqrt{x^2 + (y - y_i)^2}}{c}\right). \quad (3.5)$$

Up to now, we showed how to get the field if we know the source. Now, suppose we know the field. How can we get the source excitations? In order to achieve this, we propose a method which will be studied in the next chapter.

## Chapter 4

# GENERATION OF TIME SIGNALS BY COORDINATE TRANSFORMATION

### 4.1 Introduction

In this dissertation, we propose a holographic display device where a prescribed surface wave field pattern appears momentarily as a result of the superposition of a number of propagating waves. Each of these waves originates from one of the many electrically excited electrodes attached to the crystal. The forms of the time varying electrode signals are obtained by a mathematical inversion formula from the prescribed field.

### 4.2 Inversion Relationship

This section is taken from the *US Patent Office Disclosure Document* number 225219 [7].

Suppose that our surface is denoted as the  $(x,y)$  plane, with the upper left corner being the origin. We locate electrodes on the  $y$ -axis. From now on, assume

the variation along the  $y$ -axis is continuous, so the applied signal is given by a two-dimensional function  $f(t, y)$ . After finding the result for the continuous case, it can be easily discretized.

Let the time varying field on the crystal surface be  $\psi_t(x, y)$ . At a specific instant of time  $t_i$  we want to find the electrode signals,  $f(t, y)$ , from the surface pattern,  $\psi_{t_i}(x, y)$ .

Consider a general propagating plane wave which can be written as  $e^{j\omega t - \mathbf{k}^T \mathbf{x}}$ , where,  $\mathbf{k}$  is the wavenumber vector  $(k_x, k_y)^T$ , and,  $\mathbf{x}$  is the position vector  $(x, y)^T$ . The direction of propagation is given by  $\alpha = (\frac{k_x}{\omega}, \frac{k_y}{\omega})^T$ . The speed of propagation is  $\frac{1}{|\alpha|}$ .

Now, let the wave be multiplied by a linear phase component  $e^{juy}$  at the crystal edge. This is analogous to the diffraction of light through a prism, or by a sawtooth transparent phase grid. For a wide range of  $u$ , the plane wave continues its propagation after the edge, on the crystal surface, but now it is refracted by a linear phase component. Therefore, if the signal

$$f(t, y) = e^{j\omega t} e^{juy}$$

is applied to the electrodes, then there will be a time-varying field over the crystal surface as

$$e^{j(\omega t - k_x x + uy)}.$$

This field is shown in Fig.4.1 where  $u = 0.3$ .

As stated above, for this field to continue propagation on the crystal,  $u$  should satisfy the constraint shown below.

$$speed = \frac{1}{|\alpha|} = c = \frac{|\omega|}{\sqrt{k_x^2 + k_y^2}}. \quad (4.1)$$

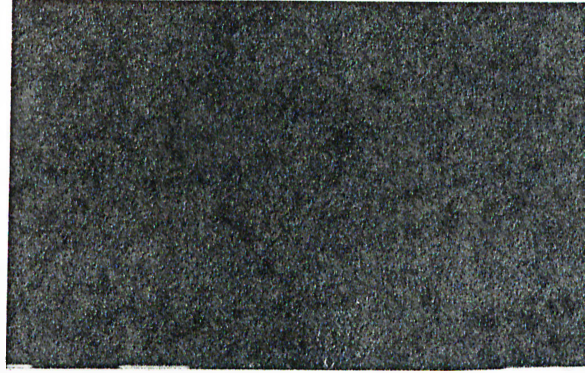


Figure 4.1: Time-varying field  $e^{j(\omega t - k_x x + uy)}$  at  $t = 0$

We know the wave number in the  $y$ -direction from the excitation as  $k_y = -u$ . So,

$$c = \frac{|\omega|}{\sqrt{k_x^2 + u^2}} \quad (4.2)$$

which yields

$$k_x = \frac{|\omega|}{\omega} \left( \frac{\omega^2}{c^2} - u^2 \right)^{\frac{1}{2}}. \quad (4.3)$$

If  $|u| > |k| = \frac{|\omega|}{c}$ , then this argument is no longer valid, since in this case the wave will not propagate on the crystal surface.

As stated above, we have the two-dimensional time-varying surface field at a specific instant of time  $t_i$ , i.e.,

$$\psi_{t_i}(x, y) = e^{j(\omega t_i - k_x x + u y)}. \quad (4.4)$$

From this field we want to get  $f(t, y)$ . So our problem reduces to a two-dimensional transformation. Considering the  $(t, y)$  domain as the input domain, and the  $(x, y)$  domain as the output domain, we want to transform  $\psi_{t_i}(x, y)$ , the surface field, to  $f(t, y)$ , the electrical signals applied to the electrodes. In other words, we want to get a sinusoidal input at the  $(t, y)$  domain with frequencies  $\omega$  and  $u$  respectively, from the sinusoidal output at the  $(x, y)$  domain with  $\Omega_x = -k_x$  and  $\Omega_y = -k_y$ . To find this transformation we use the well-known Fourier transform relationships[2],[3].

Suppose we want to generate an arbitrary field distribution  $\psi_{t_i}(x, y)$ . We can easily decompose this two-dimensional signal into its sinusoidal components using the Fourier transform as

$$\psi_{t_i}(x, y) = \frac{1}{4\pi^2} \int_{-\infty}^{+\infty} \int_{-\infty}^{+\infty} \Psi_{t_i}(\Omega_x, \Omega_y) e^{j\Omega_x x} e^{j\Omega_y y} d\Omega_x d\Omega_y. \quad (4.5)$$

The complex weights can be found from the Fourier transform as

$$\Psi_{t_i}(x, y) = \int_{-\infty}^{+\infty} \int_{-\infty}^{+\infty} \psi_{t_i}(x, y) e^{-j\Omega_x x} e^{-j\Omega_y y} dx dy. \quad (4.6)$$

We have shown previously that in order to get a surface field pattern  $\psi_{t_i}(x, y) = e^{j(\omega t_i + \Omega_x x + \Omega_y y)}$ , we have to apply  $f(t, y) = e^{j\omega t} e^{j\Omega_y y}$  to the electrodes.

So, in order to get  $e^{j\Omega_x x} e^{j\Omega_y y}$  we must apply  $e^{-j\omega t_i} e^{j\omega t} e^{j\Omega_y y}$  to the electrodes. Finally, it can be argued that

$$f(t, y) = \Psi_{t_i}(\Omega_x, \Omega_y) e^{j\omega(t-t_i)} e^{j\Omega_y y}$$

results in

$$\psi_{t_i}(x, y) = \Psi_{t_i}(\Omega_x, \Omega_y) e^{j\Omega_x x} e^{j\Omega_y y}$$

where  $\Psi_{t_i}(\Omega_x, \Omega_y)$  is a constant for fixed  $\Omega_x$  and  $\Omega_y$ .

Therefore, in order to get the arbitrary surface field pattern

$$\psi_{t_i}(x, y) = \frac{1}{4\pi^2} \int_{-\infty}^{+\infty} \int_{-\infty}^{+\infty} \Psi_{t_i}(\Omega_x, \Omega_y) e^{j\Omega_x x} e^{j\Omega_y y} d\Omega_x d\Omega_y$$

we must have

$$f(t, y) = \frac{1}{4\pi^2} \int_{-\infty}^{+\infty} \int_{-\infty}^{+\infty} \Psi_{t_i}(\Omega_x, \Omega_y) e^{j\omega(t-t_i)} e^{j\Omega_y y} d\Omega_x d\Omega_y. \quad (4.7)$$

From Eq.4.2 we know that

$$|\omega| = c\sqrt{k_x^2 + k_y^2}.$$

Hence,

$$\omega = \begin{cases} c\sqrt{k_x^2 + k_y^2} & \text{if } \Omega_x \leq 0 \\ -c\sqrt{k_x^2 + k_y^2} & \text{if } \Omega_x > 0 \end{cases} \quad (4.8)$$

or, equivalently,

$$\omega = \frac{-|\Omega_x|}{\Omega_x} c\sqrt{\Omega_x^2 + \Omega_y^2}. \quad (4.9)$$

The reason for the change in the sign of  $\omega$  due to  $\Omega_x$  is that the wave propagates away from the excitation electrodes, i.e., always in the positive  $x$ -direction.

By substituting Eq.4.9 in Eq.4.7 we get

$$\begin{aligned}
f(t, y) &= \frac{1}{4\pi^2} \int_{-\infty}^{+\infty} \int_{-\infty}^{+\infty} \Psi_{t_i}(\Omega_x, \Omega_y) e^{j\frac{-|\Omega_x|}{\Omega_x} c\sqrt{\Omega_x^2 + \Omega_y^2}(t-t_i)} e^{j\Omega_y y} d\Omega_x d\Omega_y \\
&= \frac{1}{4\pi^2} \int_{-\infty}^{+\infty} \int_{-\infty}^{+\infty} \Psi_{t_i}\left(\frac{-|\omega|}{\omega} \sqrt{\frac{\omega^2}{c^2} - \Omega_y^2}, \Omega_y\right) \frac{-|\omega|}{c^2 \sqrt{\frac{\omega^2}{c^2} - \Omega_y^2}} \\
&\quad e^{j\omega(t-t_i)} e^{j\Omega_y y} d\Omega_y d\omega.
\end{aligned} \tag{4.10}$$

If we represent  $f(t, y)$  in terms of its sinusoidal components by using the Fourier transform, we get

$$f(t, y) = \int_{-\infty}^{+\infty} \int_{-\infty}^{+\infty} F(\omega, u) e^{j\omega t} e^{ju y} du d\omega. \tag{4.11}$$

As a result if we compare Eq.4.10 and Eq.4.11 we get

$$F(\omega, u) \Big|_{u=\Omega_y} = \Psi_{t_i}\left(\frac{-|\omega|}{\omega} \sqrt{\frac{\omega^2}{c^2} - \Omega_y^2}, \Omega_y\right) \frac{-|\omega|}{c^2 \sqrt{\frac{\omega^2}{c^2} - \Omega_y^2}} e^{j\omega t_i} \tag{4.12}$$

where  $F(\omega, u)$  and  $\Psi_{t_i}(g(\omega, u), u)$  are the Fourier transforms of  $f(t, y)$  and  $\psi_{t_i}(x, y)$  respectively.

Therefore we can always find the unique input signal  $f(t, y)$  in order to get the specified surface field pattern  $\psi_{t_i}(x, y)$  at time  $t_i$ , and the relationship between the Fourier transforms of these two signals is as given above.

If we look at the above equations carefully we see that the bands of  $F(\omega, u)$  and  $\Psi_{t_i}(g(\omega, u), u)$  are not the same. The relationship can easily be found analytically or graphically. Fig.4.2 shows an example:  $\psi_{t_i}(x, y)$  is a bandpass signal with a rectangular passband, and the corresponding passband of  $f(t, y)$  is shown in Fig.4.3. As shown previously, the coordinate transformation is valid only for  $|u| > \frac{u}{c}$ . After the coordinate transformation we see that the band is hyperboloid.

Fig.4.4 and Fig.4.5 show the reverse coordinate transformation, i.e., the coordinate transformation from a rectangular passband in the  $(\omega, u)$  domain (Fig.4.4)

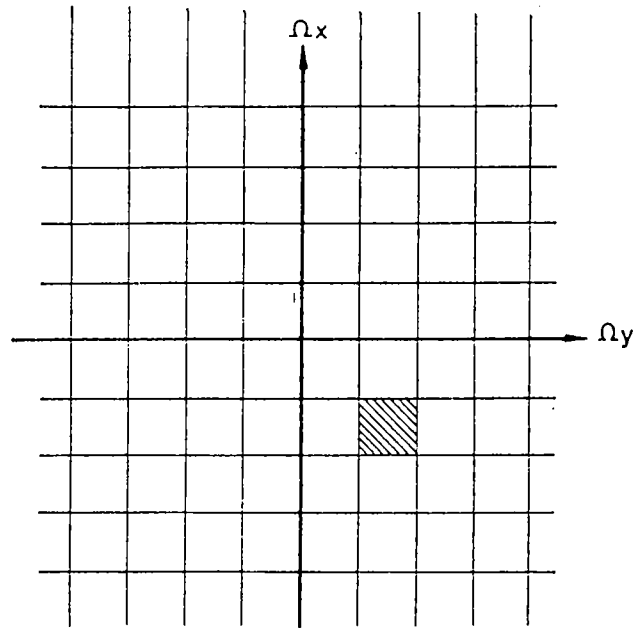


Figure 4.2:  $\Psi(\Omega_x, \Omega_y)$  with a rectangular pass-band. (Taken from [7] with the permission of the author)

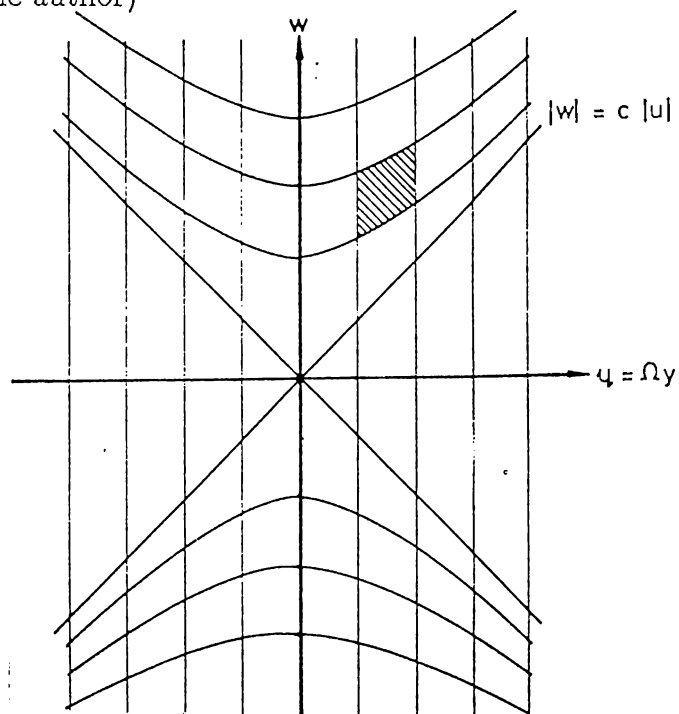


Figure 4.3:  $F(\omega, u)$  after coordinate transformation. (Taken from [7] with the permission of the author)

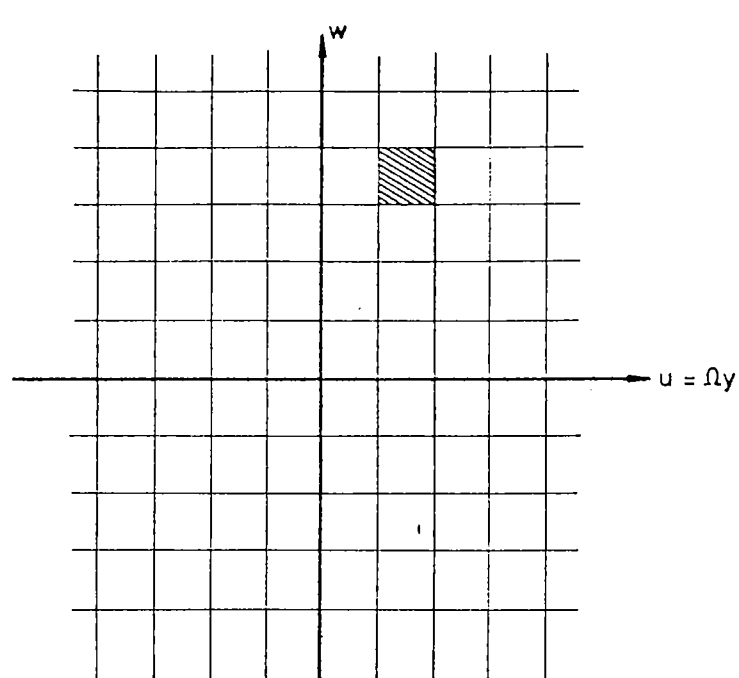


Figure 4.4:  $F(\omega, u)$  with a rectangular pass-band. (Taken from [7] with the permission of the author)

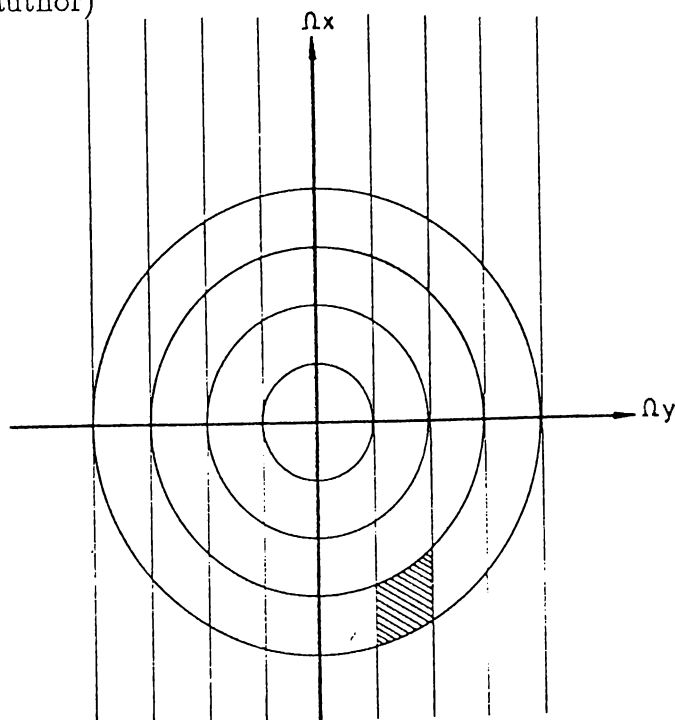


Figure 4.5:  $\Psi(\Omega_x, \Omega_y)$  after inverse coordinate transformation. (Taken from [7] with the permission of the author)

to the  $(\Omega_x, \Omega_y)$  domain (Fig.4.5).

### 4.3 Digital Processing

The inversion relationship between the source signal  $f(t, y)$  and the surface field  $\psi_t(x, y)$  is given in the previous section as a transformation between the Fourier domains  $(\omega, u)$  and  $(\Omega_x, \Omega_y)$ . In practice the length of the crystal edge where the sources are located is finite; the source is not continuous but a discrete array. In digital processing, the input surface wave pattern and the output surface wave pattern are also discrete.

Let us denote the discrete surface wave pattern as  $\psi_{t_{i_D}}(n, m)$  for  $n = 0 \dots N - 1, m = 0 \dots M - 1$ , and the discrete excitation signal by  $f(a, b)$  for  $a = 0 \dots N' - 1, b = 0 \dots M' - 1$ . One can take the DFT (Discrete Fourier Transform) of  $\psi_{t_{i_D}}(n, m)$  to get  $\Psi_{t_{i_D}}(k, l)$  as in Eq.4.13

$$\Psi_{t_{i_D}}(k, l) = \sum_{n=0}^{N-1} \sum_{m=0}^{M-1} \psi_{t_{i_D}}(n, m) e^{-j\frac{2\pi}{N}nk} e^{-j\frac{2\pi}{M}ml} \quad (4.13)$$

where  $k = 0 \dots N - 1, l = 0 \dots M - 1$ .

If there is no aliasing, the elements of this two-dimensional array are the samples of the continuous Fourier transform  $\Psi_{t_i}(\Omega_x, \Omega_y)$ . Knowing these samples, which are located on a rectangular grid, we can also find the samples of the  $F(\omega, u)$  through the relation 4.12

$$\begin{aligned} \Psi_{t_{i_D}}(k, l) &= \Psi_{t_i}(Uk, Vl) \\ &= \frac{-|Uk|}{Uk} \frac{cUk}{\sqrt{U^2k^2 + V^2l^2}} F\left(\frac{-|Uk|}{Uk} c\sqrt{U^2k^2 + V^2l^2}, Vl\right) \\ &= \frac{-|Uk|}{Uk} \frac{cUk}{\sqrt{U^2k^2 + V^2l^2}} F(k^*, l^*). \end{aligned} \quad (4.14)$$

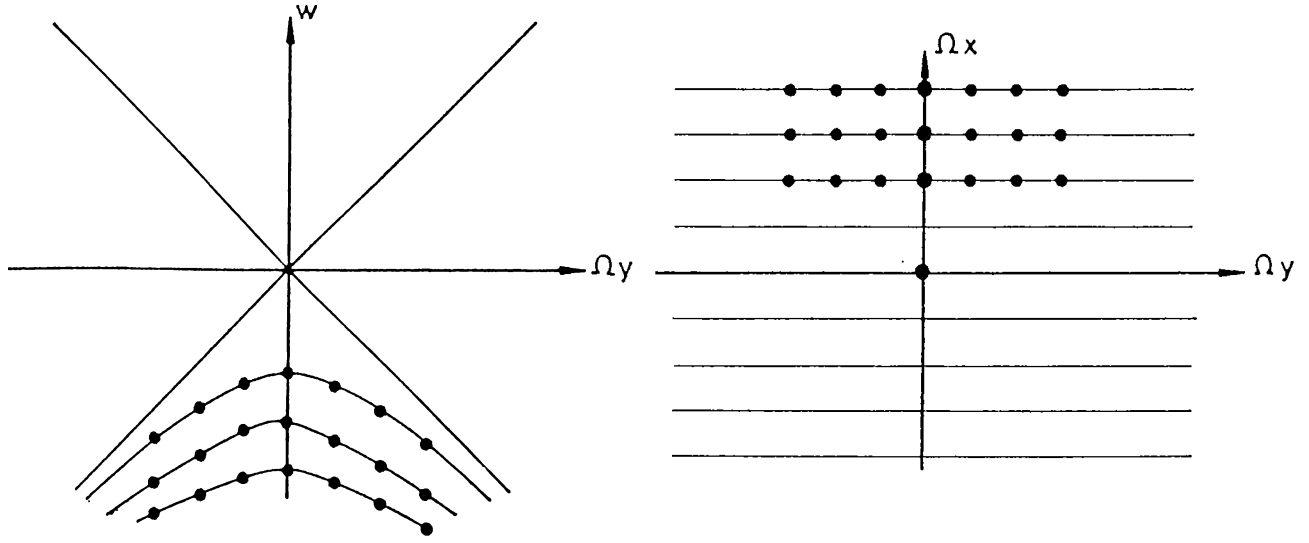


Figure 4.6: Sample locations after and before transformation

where  $0 \leq k^* < N'$ ,  $0 \leq l^* < M'$ .  $U$  and  $V$  are the sampling periods,  $c$  is the propagation speed of the wave,  $N'$  and  $M'$  are given by Eq.4.15 and Eq.4.16:

$$N' = c\sqrt{U^2(N-1)^2 + V^2(M-1)^2}, \quad (4.15)$$

$$M' = V(M-1). \quad (4.16)$$

However, the sample locations in this case do not form a rectangular grid. The locations are shown in Fig.4.6. In order to use an inverse DFT to get the discrete time signals, uniformly sampled data is required; i.e., we have to know  $F(d, e)$  for  $d = 0, \dots, N' - 1$  and  $e = 0, \dots, M' - 1$ .

This can be achieved rather easily, because the sampling in the  $u$ -direction is already uniform. A column of points, corresponding to a constant  $k = e$  (or equivalently to a constant  $u$ ) can be taken at a time, digitally interpolated by a sufficient amount first and then sampled again to get the samples of  $F(\omega, u)$  at the proper locations to form a rectangular sampling grid. Of course, the interpolation is different for each  $e$ .

After interpolation and resampling, taking the inverse DFT of  $F(d, e)$  for  $d = 0 \dots N' - 1, e = 0 \dots M' - 1$  will give us the discrete time signals  $f(a, b)$  where

$$f(a, b) = \sum_{n=0}^{N'-1} \sum_{m=0}^{M'-1} F(d, e) e^{-j\frac{2\pi}{N'}ad} e^{-j\frac{2\pi}{M'}be} \quad (4.17)$$

for  $a = 0 \dots N' - 1, b = 0 \dots M' - 1$ .

As we use DFT in computations, the time signal  $f(a, b)$  formed in simulations is intrinsically periodic in both  $a$  and  $b$  directions (Eq.4.18 through Eq.4.20). But the inversion relationship between the surface field and the time signal is derived in the continuous domain (Eq.4.12) and because of this, the time signal is of infinite extent in both variables  $t$  and  $y$ . This causes aliasing in the computed periodic time signals. The effect of aliasing can not be gotten rid of but can be decreased by zero padding the input image  $\psi(n, m)$ .

$$\psi(n, m) \iff \Psi(\omega_x, \omega_y) \quad (4.18)$$

where  $\Psi(\omega_x, \omega_y)$  is the discrete-time Fourier transform of the finite support input image,  $\psi(n, m)$ ; i.e.

$$\Psi(\omega_x, \omega_y) = \sum_{n=-\infty}^{\infty} \sum_{m=-\infty}^{\infty} \psi(n, m) e^{-j\omega_x n} e^{-j\omega_y m}.$$

As we are working in discrete domain we need the samples of  $\Psi(\omega_x, \omega_y)$ . Sampling in frequency domain yields periodic repetition of  $\psi(n, m)$  in space domain as given by Eq.4.19.

$$\Psi(k, l) = \Psi(\omega_x, \omega_y)|_{\omega_x = \frac{2\pi}{N}k, \omega_y = \frac{2\pi}{M}l} \iff \sum_i \sum_j \psi(n + Ni, m + Mj) \quad (4.19)$$

where  $N$  and  $M$  are the periods.

After coordinate transformation given by Eq.4.14 we get

$$F(d, e) = F(\omega, u)|_{\omega = \frac{2\pi}{N'}d, u = \frac{2\pi}{M'}e} \iff \sum_i \sum_j f(a + N'i, b + M'j). \quad (4.20)$$

As we have a periodic input pattern given by the righthand side of Eq.4.19, the time signal that must generate it must also be periodic as given by the righthand side of Eq.4.20, but we have overlaps in the time signal. The reason for these overlaps is the infinite extent of the time signal in both variables  $t$  and  $y$ . If one wishes to have a perfect reconstruction of the periodic pattern,  $\sum_i \sum_j \psi(n + Ni, m + Mj)$ , then an infinite array of electrodes all radiating at all times must be considered. However, we must restrict ourselves to a finite number of electrodes, i.e. a finite number of periods of the time signal in  $y$ -direction. If only one period (in  $y$ -direction) of the time signal is chosen, then all of the 2-D periods of the space pattern degrades but the degradation is less in the main period. The degradation is due to information missing because of not using all the periods.

Even though we can get a perfect reconstruction by using an infinite array of electrodes we can not get rid of the aliasing effect due to the infinite extent of the time signal. This effect can be decreased by proper choice of  $N$  and  $M$ , i.e. by zero padding the input pattern as given by Eq.4.24. If we choose  $N$  and  $M$  large enough we get

$$\psi(n, m) \approx \sum_i \sum_j \psi(n + Ni, m + Mj)$$

for the main period. So the time signal required to generate this pattern is also more concentrated on the main period.

The above procedure is implemented by using SUN workstations as follows:

- The first step is to zero pad the input image, the image which will be on the crystal at a given instant as a result of the propagation of the electrode signals, and take the 2-D  $N \times M$  discrete Fourier transform. The Fourier transform is taken by using a Radix 4 transform (App. B). The real and imaginary parts are stored separately.
- If the original signal has a DC value, it must be suppressed because the magnitude after the coordinate transformation blows up to infinity on the  $|u| = |\omega|/c$  lines which correspond to  $\psi_x = 0$  (Eq.4.12). Let us denote this lower cut-off frequency as " $l_{low}$ ."
- Now the coordinate transformation given by Eq.4.14 can be done. As stated previously, after the coordinate transformation we will have no more uniform samples. So, interpolation and resampling must be done.

Various interpolation algorithms are found in literature for both nonuniform and uniform samples [1],[5],[6],[16],[17]. The interpolation algorithms for uniform sampled data are much easier and more efficient to implement. So, in this step we did the interpolation between the samples of  $\Psi(k, l)$  which are known on a uniform rectangular grid.

In the discrete domain Eq.4.9 becomes

$$k^* = \frac{-|Uk|}{Uk} c \sqrt{U^2 k^2 + V^2 l^2} \quad (4.21)$$

where  $U, V$  are the sampling periods and  $c$  is the speed of propagation. The constant  $c$  is chosen such that the DFT size does not change after the coordinate transformation, i.e.,  $N = N', M = M'$ .

By using Eq.4.21 we can find  $d_{min}$  and  $d_{max}$  where  $d_{min} = c.l_{low}$  and  $d_{max} = c\sqrt{U.U.N/2.N/2 + V.V.M/2.M/2}$  as  $k = N/2, l = M/2$  corresponds to the highest frequency in discrete domain.

Now, we want to find the value of  $F(k, l)$  at each  $k, l$  for  $k_{min} \leq k \leq k_{max}$ . For this, we perform the inverse coordinate transformation to find the corresponding value in the  $(k, l)$  domain as

$$k' = \frac{|d|}{d} \frac{1}{U} \left( \frac{d^2}{c^2} - V^2 e^2 \right)^{\frac{1}{2}} \quad (4.22)$$

where  $0 \leq k' < N$ . As seen from Eq.4.22 the  $k'$  may not be an integer. Since the pixel values are defined only at integer values of  $k$  and  $l$ , using non-integer values causes a mapping into locations of  $\Psi$  for which no gray levels are defined. It then becomes necessary to infer what the gray level values at those locations should be, based on the pixel values at integer coordinate locations by using interpolation.

The interpolation that we used here is a combination of linear interpolation and resampling as described below [1]. There are other interpolation algorithms in the literature [5],[6],[16],[17].

- Compute the 2-D inverse DFT of the finite size sequence  $\Psi(k, l)$  of size  $N \times M$  in order to get  $\psi(n, m)$  for  $n = 0..N - 1, m = 0..M - 1$

$$\psi(n, m) = \frac{1}{NM} \sum_{k=0}^{N-1} \sum_{l=0}^{M-1} \Psi(k, l) e^{j \frac{2\pi}{N} nk} e^{j \frac{2\pi}{M} ml}. \quad (4.23)$$

- Zero pad  $\psi(n, m)$  and construct a new sequence  $\psi_{new}(n, m)$  as follows:

$$\psi_{new}(n, m) = \begin{cases} \psi(n, m) & n = 0, \dots, N/2; \\ & m = 0, \dots, M - 1 \\ \psi(n + N - LN, m) & n = LN - N/2 + 1, \dots, LN - 1; \\ & m = 0, \dots, M - 1 \\ 0 & n = N/2 + 1, \dots, LN - N/2; \\ & m = 0, \dots, M - 1 \end{cases} \quad (4.24)$$

- Perform 2-D DFT on the sequence  $\psi_{new}(n, m)$  to obtain the sequence  $\Psi(k_{new}, l)$  which is the desired interpolated version of  $\Psi(k, l)$

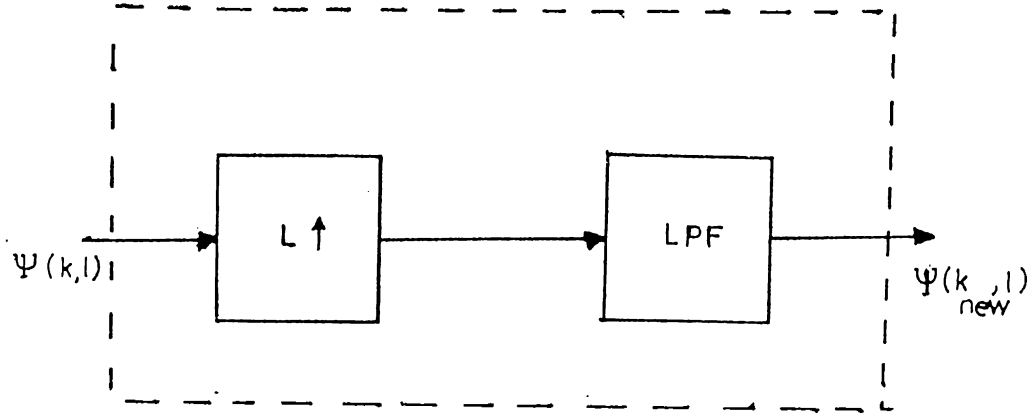


Figure 4.7: Interpolation

$$\Psi(k_{new}, l) = \frac{1}{LNM} \sum_{k=0}^{LN-1} \sum_{l=0}^{M-1} \psi_{new}(n, m) e^{j \frac{2\pi}{LN} nk} e^{j \frac{2\pi}{M} ml} \quad (4.25)$$

where  $k_{new} = 0, \dots, LN - 1, l = 0, \dots, M - 1$ .

$$\Psi(k_{new}, l) = 0$$

for  $k_{new} > LN - 1$

- The above operation is equivalent to upsampling by  $L$  and filtering of  $\Psi(k, l)$  along the  $k$ -axis in order to get more samples in this dimension [6]. The upsampling ratio is limited by the size of the arrays that can be used in SUN-workstations. The arrays which are of float type can use 8 megabytes of swap area which is the actual swap area of the system.
- Although 2-D DFT interpolation increases the sampling rate significantly, further interpolation is needed for coordinate transformation. So, at this step we perform an additional linear interpolation. The weighted average of two nearest neighbors along  $k$ -direction, along which there are no electrodes, is taken as follows.

$$\Psi(k', l) = \Psi(k_1, l)|k_1 + 1 - k'| + \Psi(k_1 + 1, l)|k_1 - k'| \quad (4.26)$$

where

$$k_1 \in Z$$

$$k' = \frac{|d|}{d} \frac{1}{U} \left( \frac{d^2}{c^2} - V^2 e^2 \right)^{\frac{1}{2}} \in R$$

$$k_1 < k' < k_1 + 1.$$

- After this interpolation scheme we get  $F(d, e)$  for each  $d, e$  in the region bounded by  $e_{min} \leq e \leq e_{max}$ . (Limits of  $d$  do not change.)
- Now we have  $F(c, d)$  which consists of uniform samples so we can take Inverse Discrete Fourier Transform. The result of Inverse Discrete Fourier Transform will give us the samples of  $f(t, y)$

$$f(a, b) = \frac{1}{NM} \sum_{d=0}^{N-1} \sum_{e=0}^{M-1} F(d, e) e^{j\frac{2\pi}{N}ad} e^{j\frac{2\pi}{M}be} \quad (4.27)$$

where  $a = 0, \dots, N - 1, b = 0, \dots, M - 1$ .

## 4.4 Results

In our simulations we chose the size of the object to be 64x128, the upsampling ratio  $L$  to be 4, the propagation speed  $c$  to be 1.0 and the sampling periods  $U$  and  $V$  to be 1.

The algorithm was applied to various images. The series of simulations shown in Fig.4.8-4.12 show the effect of spurious response due to the periodicity of the computed time signals. Fig.4.8 is the original input pattern. Fig.4.9 is the computed time signals when the input object is extended to a 128x128 image by zero-padding

and Fig.4.10 is the one when the input object is extended to a 256x256 image again by zero-padding. When these time signals are radiated we get Fig.4.11.a and Fig.4.11.b respectively. The effect of periodicity on the reconstructed pattern can easily be seen from these figures. When we pad the input pattern by more zeros we decrease the effect the portion of the time signal which causes aliasing; i.e. the portion of the time signal related to the other periods of the input image. As the whole information about the input object forms only a small portion of the input pattern after zero padding, the related time signal has also most of the information concentrated in a limited region. We can still get a better reconstruction by using more than one period of time signal in radiation. As each period contains extra information, when the number of periods in radiation increases, our approximation converges to the ideal case where the time signal is of infinite length and the pattern generated by the radiation of this time signal is the periodically repeated version of the input pattern. Fig.4.11.c shows the reconstructed pattern where 5 periods of the time signal in  $y$ -direction are used in radiation. The time signal is repeated in  $t$ -direction until the input pattern is generated as in the previous cases. When the number of periods increases we get a better reconstruction but the computation time increases enormously.

Two other series of simulations are shown in Fig.4.12 through Fig.4.15.

Fig.4.16 through Fig.4.21 show the relation between the number of electrodes and resolution. The two points in Fig.4.16 are one pixel apart from each other. Fig.4.17 is the time signal for 128 electrodes, and Fig.4.18 is the time signal for 256 electrodes. When these time signals are radiated we get Fig.4.19 and Fig.4.20, respectively. It is seen from Fig.4.19 to Fig.4.20 that we can get the resolution given in Fig.4.16 by using 256 electrodes.

The output images are shown using a common intensity scale and each point is represented by an 8-bit intensity level.

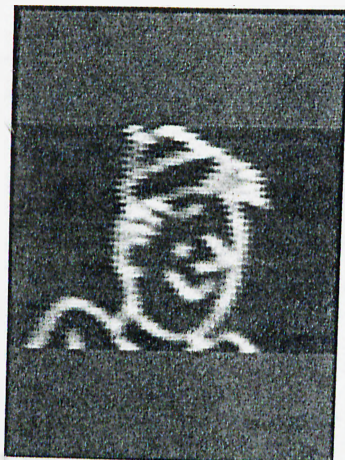


Figure 4.8: Input object pattern

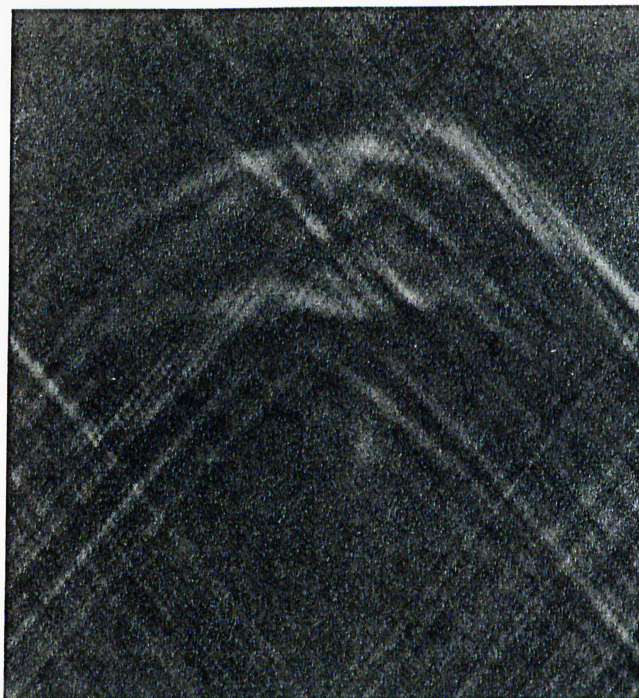


Figure 4.9: Computed time signals after extension to 128x128 image

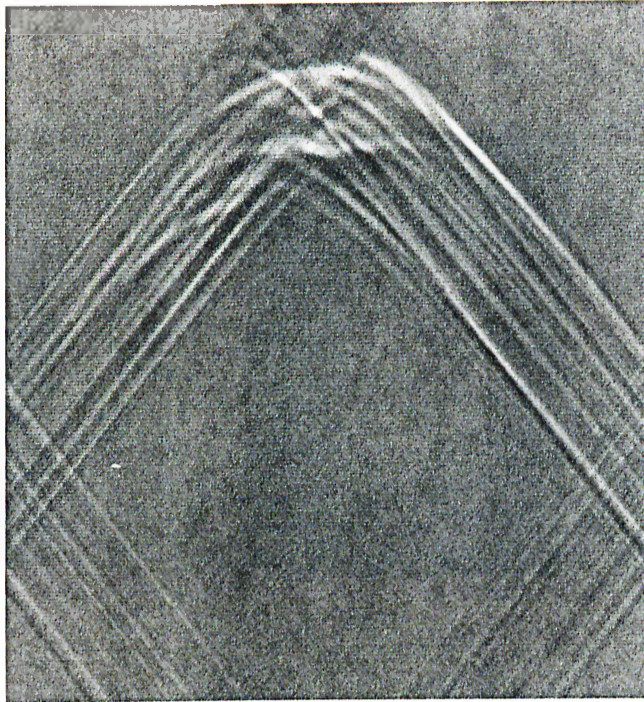


Figure 4.10: Computed time signals after extension to 256x256 image

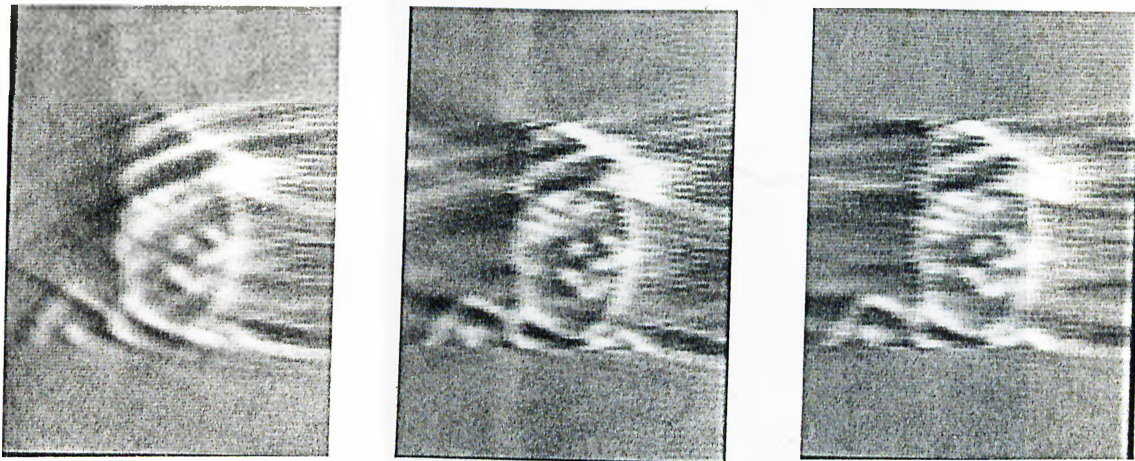


Figure 4.11: Reconstructed objects (a) by radiating the time signal in Fig.4.9, (b) by radiating the time signal in Fig.4.10, (c) by periodically radiating the time signals in Fig.4.10



Figure 4.12: Input object pattern and reconstructed object after radiation of time signal in Fig.4.13

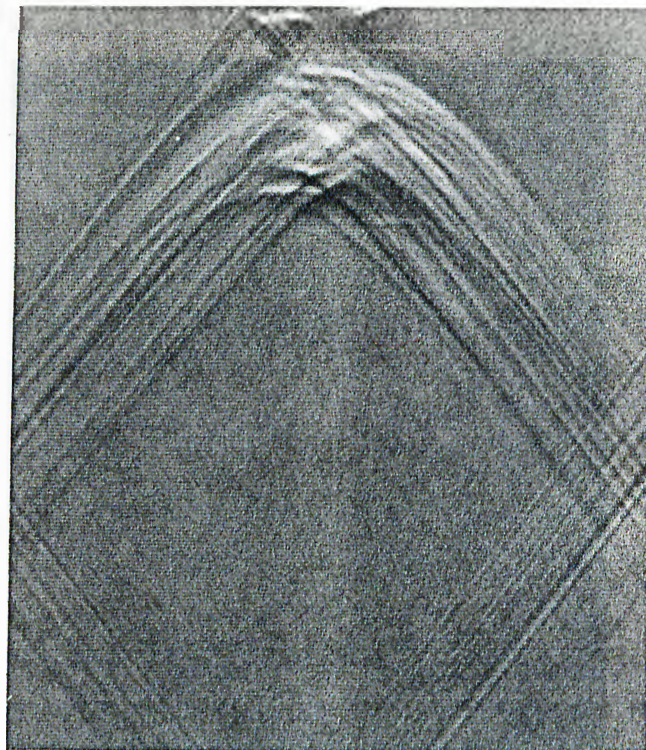


Figure 4.13: Computed time signals

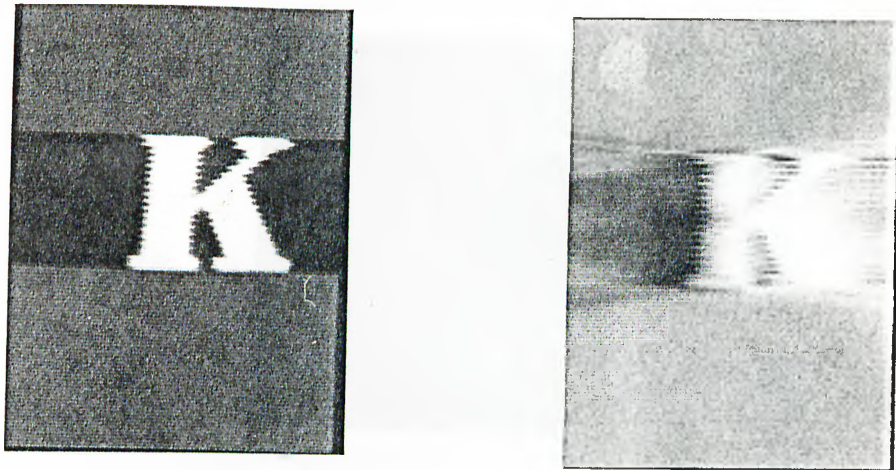


Figure 4.14: Another input object pattern and reconstructed object after radiation of time signal in Fig.4.15

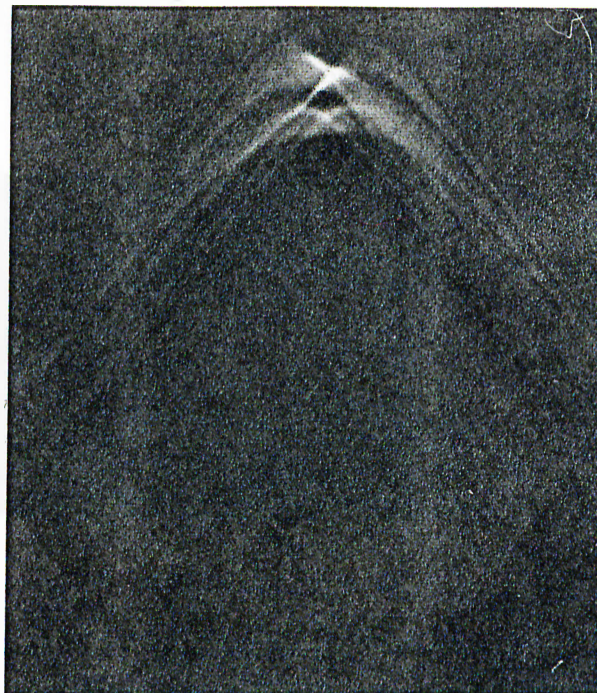


Figure 4.15: Computed time signals

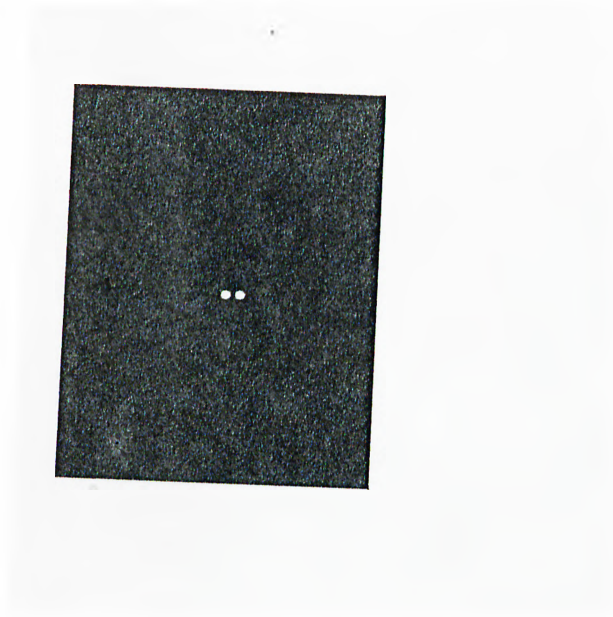


Figure 4.16: Input pattern to show the relation between the resolution and the electrode number

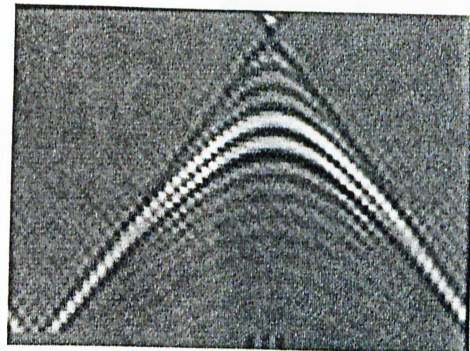


Figure 4.17: Computed time signals for 128 electrodes

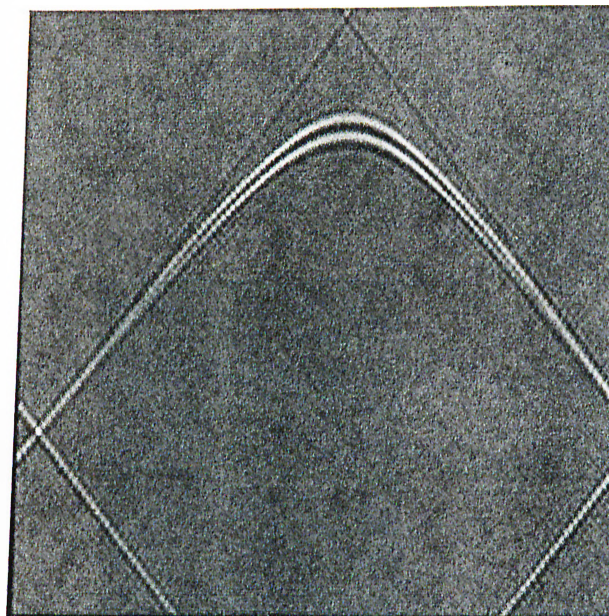


Figure 4.18: Computed time signals for 256 electrodes

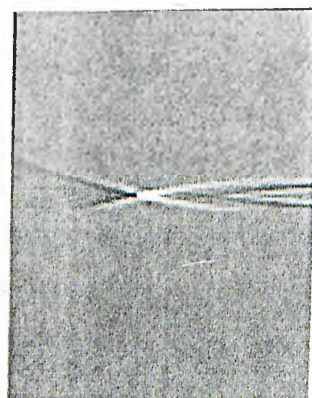


Figure 4.19: Reconstructed object after radiation of time signal in Fig.4.17

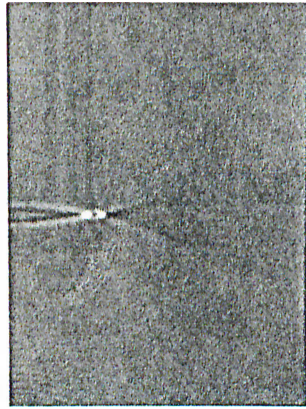


Figure 4.20: Reconstructed object after radiation of time signal in Fig.4.18

## Chapter 5

### A PRACTICAL IMPLEMENTATION

The algorithms presented in the previous sections can be used to develop a three-dimensional acousto-optic television display [7].

The principle of operation is based on forming the holographic pattern, for a short duration of time, on a crystal using propagating surface waves, and illuminating the so-formed hologram at the proper instant by a coherent light pulse to reconstruct the associated wavefront which yields a three-dimensional frame.

The propagating surface waves are generated by a number of electrodes on one side of the crystal. The electrical signals applied to these electrodes are derived from the desired hologram pattern using the inversion relation presented in Chap.4. Consecutive frames can be written easily on the crystal, and with a proper rate of repetition, a continuous three-dimensional motion picture can be observed.

In Fig.5.1, a possible three-dimensional holographic television system which utilizes the above technique is shown. At the transmitter side, there is a video camera 1 which captures the two-dimensional hologram pattern in front of it. The hologram represents the three-dimensional scene as seen by the camera. The hologram pattern captured by the camera is converted into electrical video signal and then transmitted through a channel 2 to the receiver. The received video signal

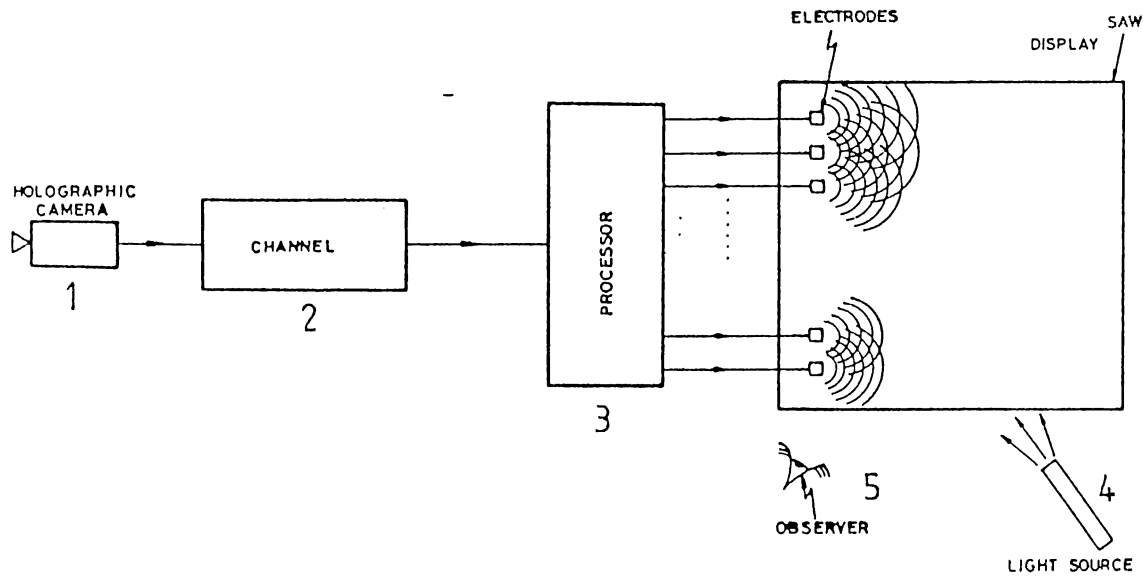


Figure 5.1: A practical implementation

is then processed by the block labeled “processor” 3. This processor performs the previously mentioned mathematical inversion processes to get the electrode signals. These electrode signals then generate the time-varying field pattern on the crystal surface, which is indeed a surface acoustic wave device (SAW) [20]. The time-varying field will yield a reproduction of the hologram in front of the video camera at a time instant  $t_0$ . Right at this time, a pulse of coherent light, may be from a laser 4, is passed through the crystal, to reconstruct the three-dimensional scene, seen by the camera, in front of the observer 5. Since there is no need to erase the written hologram explicitly, the system is ready for another frame in a short time where this duration is limited only by the propagation speed of the surface waves on the crystal. If consecutive frames are sent frequently enough, as in conventional television, the observer will see a three-dimensional motion picture.

## Chapter 6

### RESULTS

The simulation of three-dimensional holographic television display was carried out by using the algorithms given in the previous chapters for various input patterns.

Fig.6.1 shows the 64x128 2D *flower* pattern,  $a(n, m)$  and the simulated hologram of this pattern. Fig.6.2 is the time signal generated by using the method described in Chap.5. Here, the vertical axis is the “electrode axis”, whereas the horizontal axis is time. If these signals are applied to the electrodes, the propagating waves from each electrode will superpose to generate the pattern shown in Fig.6.3 at a specific instant. Here, the desired result is to have Figures 6.1.b and 6.3 exactly equal to each other. However, due to propagation (and some computational errors such as round off noise) the two pictures will be slightly different. Using this new pattern as the hologram (which would be on the surface of the SAW -surface acoustic wave- device), the original object (which is a 2-D, i.e., flat pattern in 3-D space for this figure) can be reconstructed as in usual holography. This will be done optically in the real system, but here the reconstruction result is obtained through simulation. This is shown in Fig.6.4.a. For comparison, the same simulation method is applied to the original hologram of Fig.6.1.b. The result of this simulation is shown in Fig.6.4.b.

Another series of images are shown in Figures 6.5-6.8. In these simulations,

the input images are first extended to 256x256 images and 5 periods of generated time signals for 256 electrodes are used in reconstruction.

A series of simulations shown in Fig.6.9-6.13 are different. The simulated object in this case is 3-D: there are two squares (each is a 2-D object), but they are located at different depths (the third dimension). Again, the reconstructions are simulated both from the original hologram and the hologram obtained from the propagation of the acoustical waves from the electrodes. Since there are two different depths, two different reconstructions, each focusing at a different object are shown. The results are very satisfactory.

The simulations were carried out by using SUN-3/110 deskside color workstation which is a 32-bit system based on Motorola MC68020 CPU chip and the high-speed 32-bit VME bus. The operating system is the enhanced version of UNIX. The main memory is eight megabytes and there are 256 simultaneously displayed colors. The hardware also includes a coprocessor MC6881. The system has a window-based user environment to exploit the capabilities of the high-resolution 1152x900 bit-mapped screen. The display of gray level images is performed by using the windows and pixwins (related to pixels) to access the specific portion of the screen defined by windows.

The simulation programs were written in C, which is a general purpose language, designed for structured programming. For display purposes, the results of the computations are converted to 256 gray level images. For all of the pictures, this is done by assigning the lowest pixel value to 0, and the highest one to 255. This assures the maximum use of the dynamic range of the gray image.

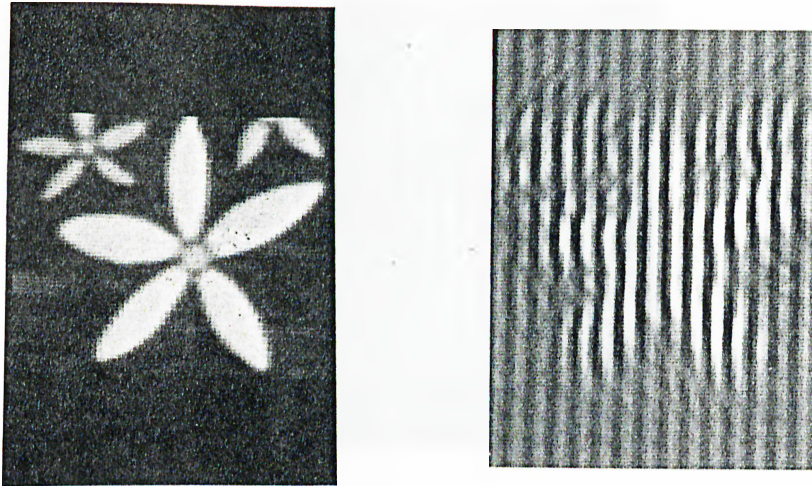


Figure 6.1: (a)The 64x128 2D *flower* pattern and (b)the simulated hologram of this pattern

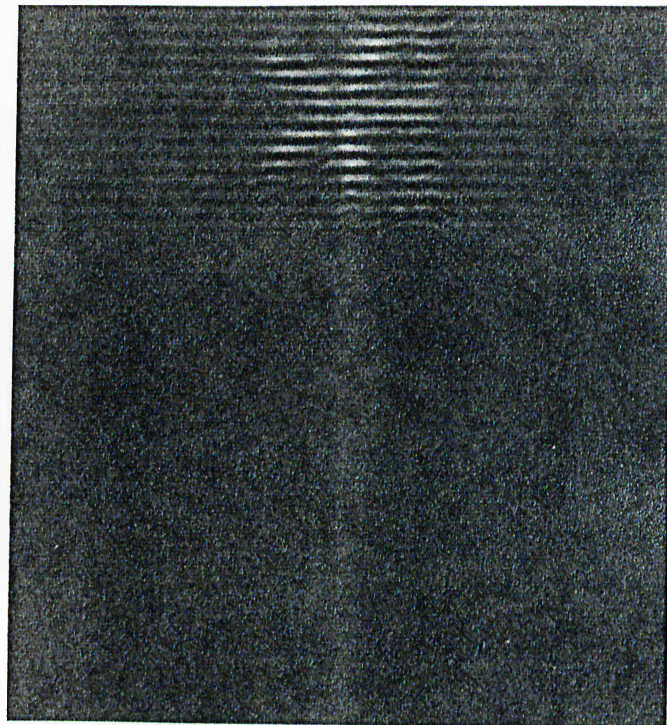


Figure 6.2: The computed time signal

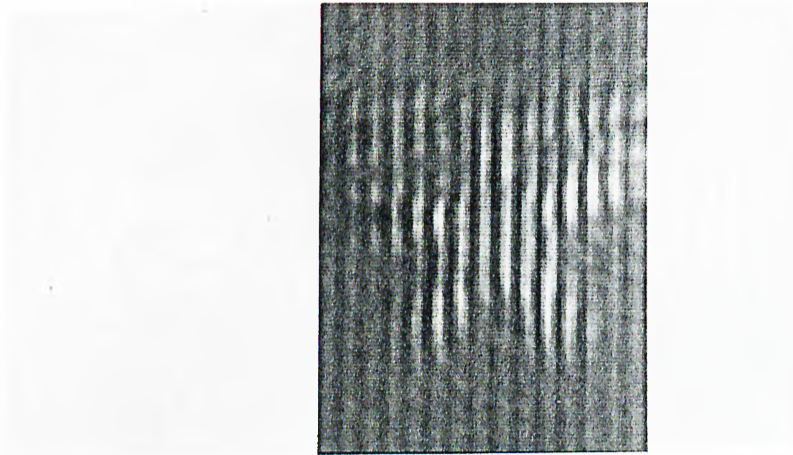


Figure 6.3: The reconstructed hologram after radiation of time signal in Fig.6.2

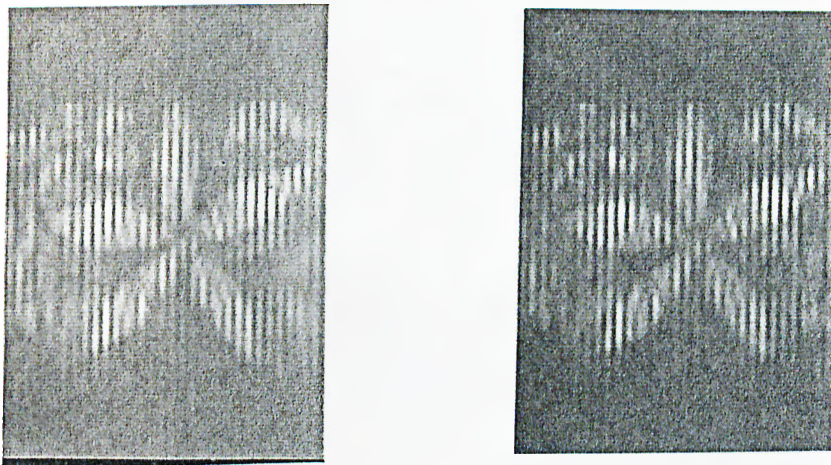


Figure 6.4: Reconstruction from holograms (a) in Fig.6.1.b and (b) in Fig.6.3

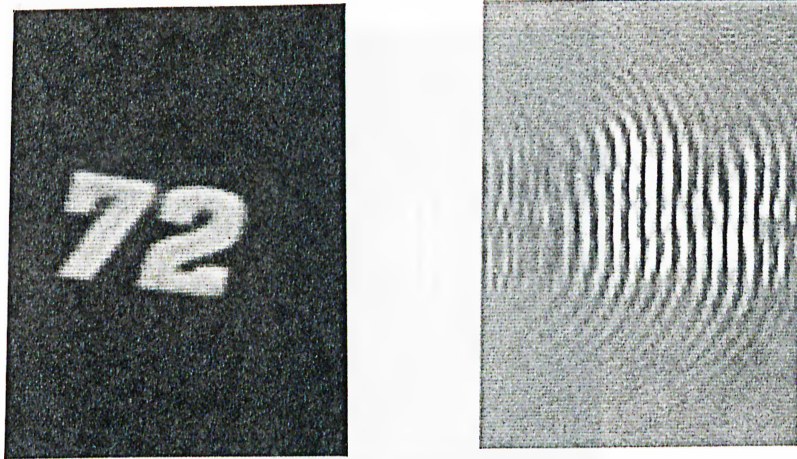


Figure 6.5: (a) Another input pattern and (b) the simulated hologram of this pattern

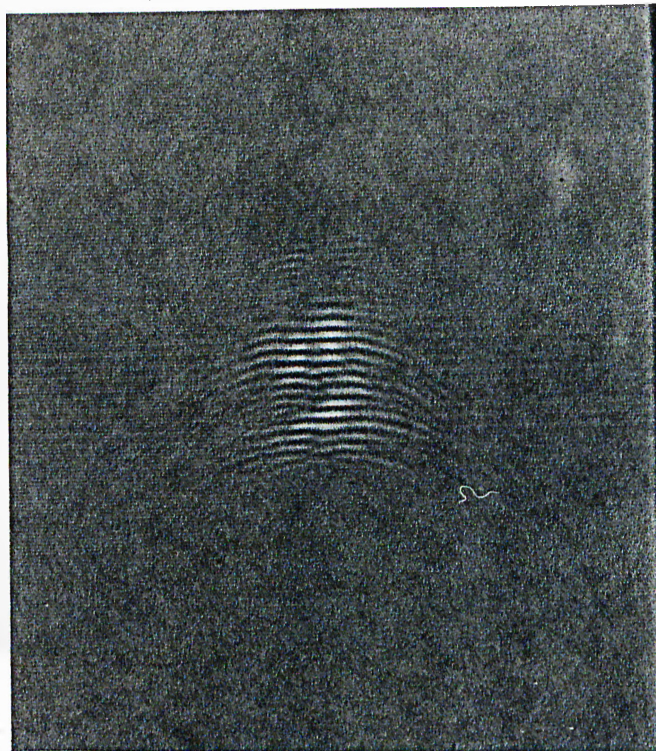


Figure 6.6: The computed time signal

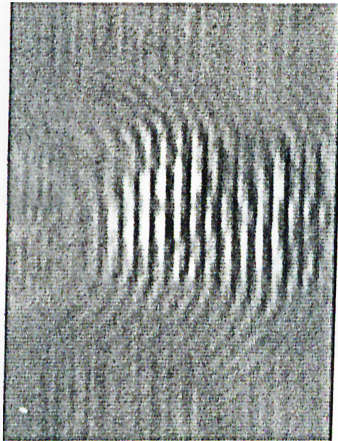


Figure 6.7: The reconstructed hologram after radiation of time signal in Fig.6.6

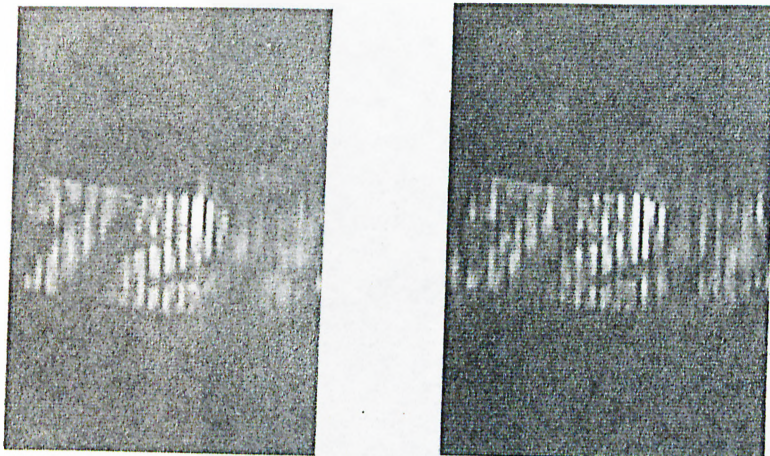


Figure 6.8: Reconstruction from holograms (a) in Fig.6.5.b and (b) in Fig.6.7

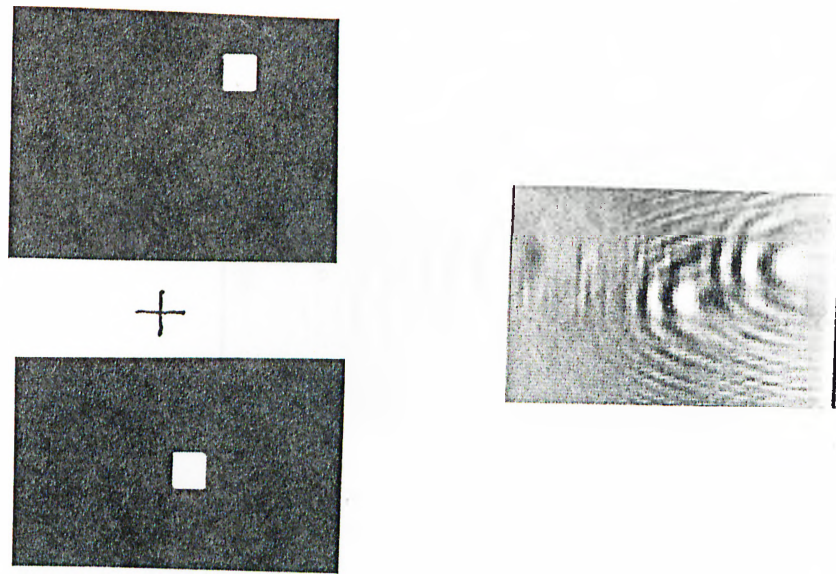


Figure 6.9: (a) A 3D input pattern and (b) the simulated hologram of this pattern



Figure 6.10: The computed time signal



Figure 6.11: The reconstructed hologram after radiation of time signal in Fig.6.10

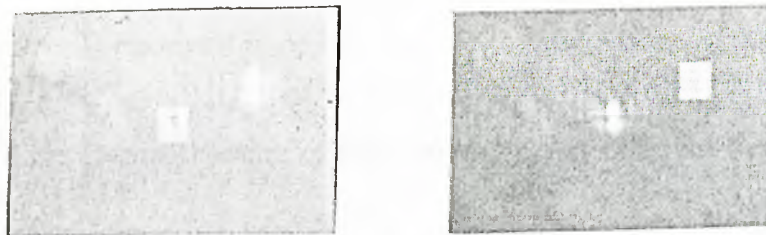


Figure 6.12: Reconstruction of the two objects at different depths from the hologram in Fig.6.9.b



Figure 6.13: Reconstruction of the two objects at different depths from the hologram in Fig.6.11

## Chapter 7

### HOW TO USE THE SIMULATOR

The simulation programs implement six different tasks such as system function generation for holography, conventional off-axis holography, reconstruction from hologram, time-signal generation, wave propagation on the crystal and the display of the created images.

All the programs have standard input/output formats which have four bytes of header in front of the actual floating-point data. The header contains the input data sizes of the  $x$  and  $y$  coordinates. The programs are interactive. They all ask for inputs such as filenames and certain parameters by prompting with a suitable explanation.

#### 7.1 Example

Suppose that the image file `object.img` has already been generated by using the standard input/output format found in SUN workstations (App. C). In order to take its hologram, to find the time signals and to radiate them, to reconstruct the object back and to display the resultant images the following sequence of main programs must be executed.

1. Run `hssystem` to find the system function  $h_{zD}(n, m)$  given by Eq.2.18.

`>hssystem`

*Enter the size of the data (x,y): 64 128*

*Enter the factor alpha: 10 (\* alpha is related to the distance z and given by Eq.2.17 \*)*

*Enter the output filenames (real, imaginary): hreal himag (\* These are the names of the file that will contain the real and imaginary parts of the system function for the given sizes and alpha \*)*

2. Run `offuser` to take the hologram of `object.img`.

`>offuser`

*Enter the input filename: object.img*

*Enter the name of the real part of the system function: hreal*

*Enter the name of the imaginary part of the system function: himag*

*Enter the factor beta: 10 (\* Beta is given by the Eq.2.19 \*)*

*Enter the output filename: hologobject (\* hologram of object.img is stored in the file named hologobject \*)*

*Do you want to use another hologram with different z? (yes- >1) 0 (\* If 3-D holography is wanted to be simulated one must go through the above steps once more by entering 1 at this instant. This time new system function with different alpha must be used. The output contains the addition of the two holograms taken at different distances. \*)*

3. Run `interuser` to perform the coordinate transformation and find the time signals.

`>interuser`

*Enter the input filename: hologobject*

*Enter the name of the time signal: time1 (\* The computed time signals which will regenerate the input image after radiation is stored in the file named time1 \*)*

4. Run `raduser` to radiate the given time signals.

```
>raduser
```

*Enter the name of the time signal: time1*

*Do you want periodic repetition? (yes— >1) 0* (\* If periodic extension of the time signal is wanted to be radiated 1 must be entered at this step. If 1 is entered the number of repetitions will also be asked. \*)

*Enter the name of the reconstructed pattern: recons1* (\* The pattern after radiation of the time signals is stored in the file named recons1. \*)

5. Run `reconuser` to reconstruct the original object back from the holographic pattern `recons1`.

```
>reconuser
```

*Enter the input filename: recons1*

*Enter the name of the real part of the system function: hreal*

*Enter the name of the imaginary part of the system function: himag*

*Enter the output filename: recobject* (\* reconstruction from the hologram `recons1` is stored in the file named `recobject` \*)

*Do you want to reconstruct the other object? (yes— >1) 0* (\* If superposition of holograms of different objects at different distances are used in part 3 than these objects can be reconstructed by entering 1 at this step, i.e., going through the above steps by using appropriate system functions. \*)

6. Run `plot` to display any output file with standard format.

```
>plot recobject (* plots the contents of the file named recobject *)
```

## Chapter 8

### CONCLUSION

In this dissertation, we presented a technique for the display end of a holographic three-dimensional television system and carried out the computer simulations. The technique is based on the reproduction of the hologram using traveling surface waves. Our primary objective is to provide a simple but effective three-dimensional holographic television display.

The inversion relationship that is used to find the time signals that generate the traveling surface waves is first derived in the continuous domain. But, in practice, the length of the crystal edge where the sources are located is finite. Furthermore, the source is not continuous, but a discrete array. In simulations, these effects cause undesired responses in the reconstruction process. We show in chapter 4, section 3, how to decrease these undesired responses by changing the number of electrodes where the number of electrodes is related to both the size of the input pattern and the number of periods of time signal used for radiation. It is shown in chapter 4 that increasing the number of electrodes has a definite effect on the resolution. Let us consider only one period of the space pattern  $\psi(n, m)$  (the main period) which will be generated by the traveling waves. When more periods of the time signal in  $y$ -direction are used for radiation we get a better reconstruction, but the marginal gain decreases as the number of periods increases because of the new information that is added to the time signals lessens.

Another point to be mentioned is that, the simulations on holograms show that even if the aliasing is detectable on the generated hologram pattern, it is not visible on the reconstructed image from this hologram. The reason for this is the convolution with  $h(x, y)$  where

$$h(x, y) = \frac{1}{j\lambda z} e^{j\frac{\pi}{\lambda z}(x^2+y^2)}$$

in the reconstruction step from hologram (Eq.2.15). The convolution is indeed an integration so the impulsive errors in the holographic pattern disperses after the convolution operation.

As a result of simulations, we see that the proposed system will work as desired. The system will also be expected to solve the resolution problem in holographic displays which is limited to the resolution requirements of the optical-to-optical transducers in today's systems, and in which the reproduction of hologram is based on the signals which represent the hologram itself. In our system as we do not use the hologram itself but the time signals, we are not restricted by the resolution requirements of optical-to-optical transducers. The same principle can also be used for color as well as monochrome 3-D television by using proper light pulses and hologram patterns.

When implemented in real time, the system will be expected to differ from the simulation results in some aspects. In simulations, the reflections from the edges of the crystal are neglected, and also the number of electrodes is varied without considering physical limitations. On the other hand, in real time implementation the errors due to round off,...etc will no more effect the resultant pattern as in simulations. So if the necessary number of electrodes can be used and the information content of the input image is mainly distributed in the middle, we can say that the real time system will work as shown by the simulation results.

## Appendix A

### FOURIER TRANSFORM PROPERTIES

1. Convolution :

$$x(t) * y(t) \longleftrightarrow X(\omega)Y(\omega)$$

2. Time and frequency shift :

$$x(t - t_o) \longleftrightarrow X(\omega)e^{-j\omega t_o}$$

$$e^{-j\omega_o t}x(t) \longleftrightarrow X(\omega - \omega_o)$$

3. Symmetry property :

$$x(t) : real \longleftrightarrow X(\omega) = X^*(-\omega)$$

## Appendix B

### CALCULATION OF THE DISCRETE FOURIER TRANSFORM

The DFT sum can be written as [3],[9]

$$X(k_1, k_2) = \sum_{n_1=0}^{N_1-1} \left[ \sum_{n_2=0}^{N_2-1} x(n_1, n_2) e^{-j \frac{2\pi}{N_2} n_2 k_2} \right] e^{-j \frac{2\pi}{N_1} n_1 k_1} \quad (\text{B.1})$$

The quantity in the brackets is a 2-D sequence which we shall denote  $G(n_1, k_2)$ . Equation B.1 can then be expressed as the pair of relations

$$G(n_1, k_2) = \sum_{n_2=0}^{N_2-1} x(n_1, n_2) e^{-j \frac{2\pi}{N_2} n_2 k_2}, \quad (\text{B.2})$$

$$X(k_1, k_2) = \sum_{n_1=0}^{N_1-1} G(n_1, k_2) e^{-j \frac{2\pi}{N_1} n_1 k_1}. \quad (\text{B.3})$$

Each column of  $G$  is the 1-D DFT of the corresponding column of  $x$ . Each row of  $X$  is the 1-D DFT of the corresponding row of  $G$ . Thus we can compute a 2-D DFT by decomposing it into row and column DFTs; we first compute the DFT of

each column of  $x$ , put the results into an intermediate array, and then compute the DFT of each row of the intermediate array.

For computing 1-D DFT a "divide and conquer" strategy is used. If the DFT length,  $N$  is a power of two, the DFT can be expressed as a combination of two half-length DFTs, each of which can be expressed in turn as a combination of two quarter-length DFTs, and so on. Algorithms in which the decomposition is based on decomposing the sequence into successively smaller subsequences, are called the *decimation-in-time algorithms*. The principle can be illustrated as follows:

Since  $N$  is an even integer, we can consider computing  $X(k)$  by separating  $x(n)$  into two  $N/2$ -point sequences consisting of the even-numbered points in  $x(n)$  and the odd-numbered points in  $x(n)$ . With  $X(k)$  given by

$$X(k) = \sum_{n=0}^{N-1} x(n)e^{-j\frac{2\pi}{N}nk}, k = 0, \dots, N-1 \quad (\text{B.4})$$

and separating  $x(n)$  into its even- and odd-numbered points we obtain

$$X(k) = \sum_{r=0}^{(N/2)-1} x(2r)e^{-j\frac{2\pi}{N}2rk} + \sum_{r=0}^{(N/2)-1} x(2r+1)e^{-j\frac{2\pi}{N}(2r+1)k} \quad (\text{B.5})$$

$$= \sum_{r=0}^{(N/2)-1} x(2r)e^{-j\frac{2\pi}{N}2rk} + e^{-j\frac{2\pi}{N}k} \sum_{r=0}^{(N/2)-1} x(2r+1)e^{-j\frac{2\pi}{N}2rk} \quad (\text{B.6})$$

$$= G(k) + e^{-j\frac{2\pi}{N}k} H(k). \quad (\text{B.7})$$

Each of the sums in Eq.B.7 is recognized as an  $N/2$ -point DFT, the first sum being the  $N/2$ -point DFT of the even-numbered points of the original sequence and the second being the  $N/2$ -point DFT of the odd-numbered points of the original sequence. Although the index  $k$  ranges over  $N$  values,  $k = 0, 1, \dots, N-1$ , each of the sums need only be computed for  $k$  between 0 and  $N/2 - 1$ , since  $G(k)$  and  $H(k)$  are each periodic in  $k$  with period  $N/2$ .

As  $N/2$  is even, we can consider computing each of the  $N/2$ -point DFTs in

Eq.B.7 by breaking each of the sums in Eq.B.7 into two  $N/4$ -point DFTs, which would then be combined to yield the  $N/2$ -point DFTs. Thus  $G(k)$  and  $H(k)$  in Eq.B.7 would be computed as

$$\begin{aligned} G(k) &= \sum_{r=0}^{(N/2)-1} g(r) e^{-j\frac{2\pi}{N}2rk} \\ &= \sum_{l=0}^{(N/4)-1} g(2l) e^{-j\frac{2\pi}{N}4lk} + e^{-j\frac{2\pi}{N}2k} \sum_{l=0}^{(N/4)-1} g(2l+1) e^{-j\frac{2\pi}{N}4lk}. \end{aligned}$$

Similarly,

$$H(k) = \sum_{l=0}^{(N/4)-1} h(2l) e^{-j\frac{2\pi}{N}4lk} + e^{-j\frac{2\pi}{N}2k} \sum_{l=0}^{(N/4)-1} h(2l+1) e^{-j\frac{2\pi}{N}4lk}. \quad (\text{B.8})$$

## Appendix C

### STANDARD INPUT/OUTPUT FORMAT

In order to simplify the usage of programs, a standard file structure for input and output is necessary. In the programs developed for simulation, the outputs of one unit are usually the inputs of the next unit. This means that output files can be used as the input files at the same time. Therefore, a standard structure is necessary.

The standard file structure used for input/output has 4 bytes of header and then the floating point data. 2 bytes of header are for the input data size of  $x$ -coordinate and 2 bytes are for the input data size of  $y$ -coordinate. The floating point data is written row-wise after the header by assuming the upper left corner of the image is the  $(0, 0)$  location. For example; for an image of  $2 \times 3$  with pixel values equal to the addition of coordinate values, i.e. the value at a location  $(x_1, y_1)$  is  $x_1 + y_1$ , the standard file becomes

```
3 2 0.0 1.0 2.0 1.0 2.0 3.0
```

"

## References

- [1] S. Haykin, ed., Array Signal Processing, Englewood Cliffs, N.J.: Prentice-Hall, 1985.
- [2] J.S. Lim and A.V. Oppenheim, Advanced Topics in Signal Processing, Englewood Cliffs, N.J.: Prentice-Hall, 1988.
- [3] A.V. Oppenheim and R.W. Schaffer, Digital Signal Processing, Englewood Cliffs, N.J.:Prentice-Hall, 1985.
- [4] K. Iizuka, Engineering Optics, Springer-Verlag, Berlin, 1987.
- [5] O. Arikan, and D.C. Munson, Jr., "*Interpolation Between Two Uniform Grids*," Proc. BILCON '90, vol.2, pp.1044-1052, July 1990.
- [6] S. Mitra, "*Multirate Digital Signal Processing*," Unpublished notes, September 1988.
- [7] L. Onural, "*An Acousto-Optical Holographic Three-Dimensional Television Display*," US Patent Office Disclosure Document number 225219.
- [8] D.K. Cheng, Field and Wave Electromagnetics, Addison-Wesley Publishing Company, 1983.
- [9] D.E. Dudgeon and R.M. Mersereau, Multidimensional Signal Processing, Englewood Cliffs, N.J.:Prentice-Hall, 1984.
- [10] G. Liu and P.D. Scott, "*Phase Retrieval and the Digital Reconstruction of Holograms: Comparison of In-line and Split-Beam Holography*," Proc. 24th

- Annual Allerton Conference on Communication, Control, and Computing, pp.204-212, Oct. 1986.
- [11] E.N. Leith and J. Upatnieks, "Reconstructed Wavefronts and Communication Theory," Journal of the Optical Society of America, pp.1123-1130, 1962.
- [12] P.Hariharan, Optical Holography, Cambridge University Press, 1984.
- [13] J.E. Kasper and S.A. Feller, The Complete Book of Holograms, John Wiley & Sons, Inc., 1987.
- [14] L. Onural and P.D. Scott, "Digital Decoding of In-Line Holograms," Optical Engineering, vol.26, no.11, pp.1124-1132, Nov.1987.
- [15] J.L. Horner, Optical Signal Processing, Academic Press, Inc., 1987.
- [16] P.S.Reddy and M.N.Swamy, "Interpolation of 2-D Signals," IEEE Trans. Circuits and Systems, vol.37, no.5, May 1990.
- [17] R.E. Crochiere, L.R. Rabiner, "Interpolation and Decimation of Digital Signals-A Tutorial Review," Proceedings of the IEEE, vol.69, no.3, pp.300-331, March 1981.
- [18] R.J. Collier, C.B. Burckhardt, and L.H. Lin, Optical Holography, Academic Press, Inc., New York, 1971.
- [19] Y.I. Ostrovsky, Holography and Its Applications, Academic Press, Inc., 1977.
- [20] L.L. Baranek, Acoustics, American Institute of Physics, 1986.
- [21] J.S. Kollin, "Real-Time Display of 3-D Computed Holograms by Scanning the Image of an Acousto-Optic Modulator", Proc. of the 2nd Inter. Congress of Optical Sciences and Engineering, 1989.
- [22] P.St. Hilaire, "Electronic Display system for Computational Holography," SPIE Proc., vol. #1212 Practical Holography 4, pp.1212-1220, 1990.
- [23] G. Saksby, Practical Holography, Prentice Hall, 1988.